BNL-97291-2012-JA

THE ROLE OF CLOUD MICROPHYSICS PARAMETERIZATION IN THE SIMULATION OF MESOSCALE CONVECTIVE SYSTEMS AND ANVIL CLOUDS IN THE TROPICAL WESTERN PACIFIC

Van Weverberg, K., Vogelmann, A. M., Lin, W., Luke, E. P., Cialella, A., Minnis, P., Khaiyer, M., Boer, E. R., and Jensen, M. P.

Submitted to
Journal of Climate

Atmospheric Sciences Division/Environmental Sciences Dept.

Brookhaven National Laboratory

U.S. Department of Energy
Office of Science

DISCLAIMER

The Role of Cloud Microphysics Parameterization in the Simulation of Mesoscale Convective Systems and Anvil Clouds in the Tropical Western Pacific

K. Van Weverberg[1], A. M. Vogelmann[1], W. Lin[1], E. P. Luke[1], A. Cialella[1], P. Minnis[2], M. Khaiyer[3], E. R. Boer[4] and M. P. Jensen[1]

[1]Brookhaven National Laboratory, Upton, NY, USA

[2]National Aeronautics and Space Administration Langley Research Center, Hampton, VA, USA

[3]Science Systems and Applications, Inc., Hampton, VA, USA

[4]Entropy Control, Inc., La Jolla, CA, USA

Abstract

This paper presents a detailed analysis of convection-permitting cloud simulations, aimed at increasing the understanding of the role of parameterized cloud microphysics in the simulation of mesoscale convective systems (MCSs) in the tropical western pacific (TWP). Simulations with three commonly used bulk microphysics parameterizations with varying complexity have been compared against satellite retrieved cloud properties. An MCS identification and tracking algorithm was applied to the observations and the simulations to evaluate the number, spatial extent, and microphysical properties of individual cloud systems. Different from many previous studies, these individual cloud systems could be tracked over larger distances due to the very large TWP domain studied.

The analysis demonstrates that the simulation of MCSs is very sensitive to the parameterization of microphysical processes. The most crucial element was found to be the fall velocity of frozen condensate. Differences in these fall velocities between the different experiments were more related to differences in particle number concentrations than in fall speed parameterizations. Microphysics schemes that exhibit slow sedimentation rates for ice aloft experience a larger buildup of condensate in the upper troposphere. This leads to more numerous and larger MCSs with larger anvils. Surface precipitation was found to be overestimated and rather insensitive to the microphysical schemes employed in this study. The performances of complex two-moment schemes in terms of the investigated cloud properties were not superior to the simpler one-moment schemes, since explicit prediction of number concentration does not necessarily improve processes such as ice nucleation, the aggregation of ice-crystals into snowflakes, and their sedimentation characteristics.

1. Introduction

High clouds, particularly in the tropics, have been a challenge to climate modeling ever since its inception, even as the microphysical representation of clouds improved and spatial grid spacings became smaller over the years (Randall et al. 2003). One of the main reasons is that our basic understanding of these clouds is still rudimentary at best (Stephens 2005); yet they are known to form an inherent part of the global radiation budget. Hence progress of the reliability of climate simulations might be contingent on resolving the microphysical uncertainties surrounding tropical cirrus and convective anvils (Del Genio 2011).

A number of large observational experiments conducted over the past decade (Jensen et al. 2004; Yuter et al. 2005; May et al. 2008, Schmitt and Heymsfield 2009) have unveiled at least some of the factors controlling high tropical clouds. Luo and Rossow (2004) and Mace et al. (2006) demonstrated that about half of the tropical cirrus clouds are detrained from deep convective systems (i.e. anvil-clouds), while the other half are produced in situ, due to gravity waves or large-scale uplift. The predominant source of anvil-clouds consists of detrained ice from convective updrafts, although the long lifetime of tropical cirrus systems suggests that other processes might be involved in replenishing the particles (Ackerman et al. 1988; Luo and Rossow 2004). Anvil-clouds can be advected over 1000 km (Luo and Rossow 2004) and extend more than five times the radius of the main precipitating core (Yuan and Houze 2010). The persistence of high clouds over these large distances from the main updraft cores is highly dependent on (i) the relative humidity of the upper troposphere encompassing convection, and on (ii) the particle sublimation and particle fall speeds (which are both related to their size distributions).

General circulation models (GCMs) are known to have a poor representation of convective updrafts and mass fluxes and, so far, are not capable of explicitly precipitating ice species. Grabowski (2000) argues that GCMs also do not fully allow for small-scale and mesoscale processes to feed back to the large scale. Cloud-resolving models (CRMs), however, explicitly resolve convective updrafts and have more advanced cloud microphysics schemes and, thus, are more appropriate to the study of tropical deep convective clouds and their detrainment to anvils. CRMs can also serve as tools for improving GCM parameterizations (e.g. Liang and Wu 2005; Del Genio and Wu 2010) or can be directly used as super-parameterizations within GCMs (e.g. Khairoutdinov and Randall 2001; Benedict and Randall 2009).

Most evaluation studies for tropical convection using CRMs agree that simulated radar reflectivities in the upper troposphere (within the convective cores) are too large, while brightness temperatures are generally too small (Su et al. 1999; Blossey et al. 2007; Zhou et al. 2007; Li et al. 2008; Matsui et al. 2009; Varble et al. 2011). This is often thought to be due to abundant amounts of excessively large frozen condensate at these altitudes. Many of these studies also find an underestimation of the anvil area (or the stratiform precipitation area), which suggests that the frozen precipitation not only is excessively large, but also precipitates too effectively (Zhou et al. 2007; Blossey et al. 2007). This is consistent with the findings of recent observational studies (e.g. Heymsfield et al. 2007; Schmitt and Heymsfield 2009) that fall speeds of ice particles at cold temperatures are too fast in the parameterizations used in CRMs.

Increased computing power has allowed CRMs to adopt more complex microphysics schemes over the past decade. Although several approaches that add complexity exist, there is still much debate on the extent to which they also lead to a better representation of cloud systems and which aspects of the microphysics parameterization are most promising for model

improvement. Blossey et al. (2007) found that changes to the effective radii of the precipitation species led to improvements in the fraction of high clouds but, overall, microphysics was found to have little impact. Varble et al. (2011) found a notable of microphysics on the hydrometeor distribution, but the more complex models that include more prognostic moments of the size distributions were not superior to the simpler models in terms of cloud-top heights and radar reflectivity. Similarly, Wang et al. (2009) found that a more complex microphysics scheme overestimated cirrus clouds during dry periods compared to more simple schemes, while it produced more realistic mixed-phase clouds during convection.

Typically, the aforementioned studies were performed for rather limited domains (< 500 km × 500 km), while an important fraction of the convection in tropical regions is associated with the very large mesoscale convective systems (MCSs) that often exceed such domain sizes. To capture the life cycle of convective systems and understand how these large systems gradually decay into persistent high cirrus clouds, much larger domains are desirable. Further, to understand whether models are capable of simulating key features of organized deep convection, statistics of individual convective systems need to be evaluated. By identifying and tracking these individual cloud systems in model simulations and observations, statistics on their simulated and observed properties can be compared. Finally, while many of the aforementioned studies have great value in revealing the systematic model deficiencies that occur in CRMs, only a few of those studies have been able to pinpoint the reasons for these deficiencies. The authors feel that this is indispensable in order make sound recommendations for model improvement.

This study aims at providing further insight into the role of the parameterization of cloud microphysical processes in representing deep convective clouds and their associated anvils. To that end, three commonly used microphysics parameterizations with varying complexity have

been applied to a week-long simulation of MCSs over the entire Tropical Western Pacific (TWP) domain. An MCS identification and tracking algorithm is applied to satellite-observed and model-simulated top-of-atmosphere (TOA) brightness temperature fields. Through this approach, MCS statistics are compared among the different schemes under investigation. By means of an extensive exploration of the differences between these simulations, we were able to discern features in the microphysics parameterization that are critical for proper simulations of convective clouds and their anvils, as well as determine if and why more complex microphysics schemes yield better simulations of cloud macrophysical structure. The next section describes the model setup, experiment design and details of observed and simulated cloud fields. Section 3 discusses the results of the model evaluation and the model sensitivities to microphysics. The main conclusions are given in Section 4.

2. Model description and experiment design

2.1 Model description

The CRM used in this study is the Advanced Research Weather Research and Forecasting model (ARW-WRF) Version 3.0 (Skamarock et al. 2007), which is a three-dimensional, fully compressible, nonhydrostatic CRM. The vertical coordinate is a terrain-following hydrostatic pressure coordinate and the model uses the Runge-Kutta 3rd order integration scheme. The model was integrated for a 30 M km^2 domain, centered on the TWP, applying two-way grid nesting with two nested levels. Data from the National Center for Environmental Prediction (NCEP)

Global Forecasting System (GFS; Kalnay et al. 1990) analysis with a 1° horizontal resolution were used as initial conditions and as 6-hourly boundary conditions for the largest domain that had a 20-km grid spacing and a size of 9,000 km × 6,400 km (27° N to 27° S and 89° E to 170° E). Within this domain, a 4-km grid spacing domain was nested, covering a 6,900 km × 4,440 km domain (17° N to 20° S and 100° E to 162° E), which includes most of the TWP. While previous studies often applied smaller grid spacings, the grid spacing in this study is constrained by the very large domain size that was imposed. An overview of the model (and observation) domains is provided in Figure 1. Thirty-five vertical levels were used with a vertical spacing of 60 m near the surface, increasing to 1000 m near the upper-model boundary at 20 km. The model simulations were initialized on 25 December 2003 00 UTC and integrated for a 7 day period ending on 1 January 2004 00 UTC. This period was distinguished by many large MCSs, associated with an active Madden-Julian Oscillation (MJO) in the TWP. The first day was considered to be a spin-up period and all analysis in the following sections is for the 6-day period of 26 December 2003 00 UTC to 1 January 2004 00 UTC. The Kain and Fritsch (1993) cumulus parameterization was used in the largest domain, while convection was explicitly simulated in the smaller domain. Shortwave radiation was parameterized following Dudhia (1989) and long-wave radiation was parameterized using the Rapid Radiative Transfer Model (RRTM; Mlawer et al. 1997). Three sensitivity experiments were conducted with different microphysics parameterizations, which are further detailed in section 2.2.

2.2 Experiment design

To assess the role of the parameterization of microphysical processes in the development of large convective systems and the related high cloud fields, three simulations were performed, which applied microphysics parameterization schemes with varying complexity. Roughly in order of increasing complexity, these are the one-moment WRF Single Moment 6-category scheme (Hong and Lim 2006; further referred to as WSM6), the hybrid (two-moment cloud ice) scheme by Thompson et al. (2008; further referred to as THOM), and the full two-moment scheme by Morrison et al. (2009; further referred to as MORR).

Typically, bulk microphysics schemes in CRMs (e.g. Lin et al. 1983 and Rutledge and Hobbs 1984) include 5 hydrometeor types (cloud water, rain, cloud ice, snow and graupel), which are represented by exponential size distributions of which only one moment (usually the third moment) is related to a prognostic variable (usually the mixing ratio):

$$N_x(D) = N_{0x} \exp(-\lambda_x D_x), \tag{1}$$

where N_x is the number of particles per unit volume per unit size range (m^{-3} m^{-1}), D_x is the maximum dimension of a particle (m), and N_{0X} (m^{-4}) and λ_X (m^{-1}) are the intercept and slope of the exponential size distribution, respectively. The subscript x denotes the hydrometeor type (R, S or G for rain, snow or graupel respectively). Usually, N_{0X} is assumed to be constant, while λ_X is determined by,

$$\lambda_x = \left(\frac{a_{mx} N_{0x} \Gamma(b_{mx} + 1)}{\rho_{air} q_x} \right)^{1/(b_{mx}+1)}, \tag{2}$$

where q_x is the hydrometeor mixing ratio (kg kg^{-1}) and ρ_{air} is the air density (kg m^{-3}). The parameters a_{mx} and b_{mx} are constants for the mass-diameter (m-D) relation $m_x = a_{mx} D_x^{b_{mx}}$, which are provided in Table 1 for the microphysics scheme employed in this study.

While the above approach allows for the hydrometeor size distributions to evolve over time, N_x is constrained only by q_x, which does not allow for generally observed behavior such as size sorting or aggregation (Van Weverberg et al. 2012a). To address this limitation, a number of schemes have been developed that include non-constant N_{0X} diagnosed from other prognostic variables, such as temperature (Reisner et al. 1998; Hong et al. 2004; Thompson et al. 2004). WSM6 for instance, includes a temperature-dependent N_{0S}, while all other hydrometeors still have constant N_{0X}. THOM is more advanced than WSM6 in that it includes diagnostic N_{0X} for all precipitating hydrometeors (rain, snow, and graupel). Other schemes, such as MORR, were developed to account for this in a more advanced way, by explicitly predicting N_x along with q_x (two-moment schemes; Ferrier 1994; Seifert and Beheng 2005; Morrison et al. 2009). Note that the MORR scheme used in our simulations is one-moment for cloud water and hence does not predict the N_C.

The three schemes that we applied also vary considerably in the way that they treat cloud-ice particles and their initiation. While WSM6 only predicts one moment (q_I) of the ice size distribution (and diagnoses N_I from q_I, following a power law), THOM and MORR explicitly predict two moments of the distribution (q_I and N_I). The number of ice nuclei available for ice initiation is dependent on temperature in all three schemes, but WSM6 and MORR allow new crystals to nucleate as soon as supersaturation with respect to ice is achieved at any below-freezing temperature, while THOM also requires that a supersaturation of 20% must be reached before nucleation starts.

Apart from differences in the process formulations for the conversions from one hydrometeor into another, further differences between the three schemes include the fall-speed relations used for each specie. Some schemes have a fast fallout of hydrometeors, while others have slower sedimentation velocities. Generally, bulk fall speeds of each species are given by:

$$V_x = \frac{a_{vx}\Gamma(b_{mx} + b_{vx} + 1)}{\lambda_x^{b_{vx}}\Gamma(b_{mx} + 1)}, \quad (3)$$

where the parameters a_{vx} and b_{vx} are empirical constants obtained from observed velocity-diameter (V-D) relations. Table 1 provides these constants for each of the microphysics schemes employed here. An overview of the theoretical relations of fall speed versus particle diameter is provided in Figure 2. All major size distribution characteristics and a number of other key differences between the three schemes are also provided in Table 1.

2.3 Observational data and cloud tracking

2.3.1 Observed and simulated cloud properties

To evaluate the cloud properties in all the simulations, we applied the approach of the International Satellite Cloud Climatology Project (ISCCP) to sort clouds into nine classes according to their cloud-top pressure (CTP) and cloud optical thickness (COT) (Rossow and Schiffer 2001). These classes include cirrus (Ci), cirrostratus (Cs), cumulonimbus (Cb), altocumulus (Ac), altostratus (As), nimbostratus (Nb), cumulus (Cu), stratocumulus (Sc) and stratus (St). Thresholds in CTP were used to separate low and middle cloud (680 hPa) and

middle and high cloud (440 hPa) in the satellite and the simulations. Thin, intermediately thick, and thick clouds were separated by COT thresholds of 3.6 and 23, respectively.

Hourly satellite data were used from the Geostationary Operational Environmental Satellite (GOES-9) at 4-km resolution, but sampled to achieve an effective resolution of 8 km. Observed CTP and COT were derived using the Visible Infrared Shortwave-infrared Split-window Technique (VISST), developed at the National Aeronautics and Space Administration (NASA) Langley Research Center (LaRC) and documented in Minnis et al. (2008, 2011). VISST is a four-channel, model-matching method that matches observed radiances to theoretical model calculations for a number of water and ice crystal size distributions. As the visible channel is required to determine COT, only grid cells with a solar zenith angle < 70° have been included in our analysis. Satellite data are available over most of the TWP domain, which covers an area ranging from 10° N to 20° S and 120° E to 180° E. This is slightly more eastward than the model simulation domain (Fig. 1) and in all further satellite-model comparisons we use only the 15 M km^2 area common between the satellite and the simulations (10° N to 17° S and 120° E to 162° E).

COT in the model simulations is calculated off-line for each hydrometeor separately, following a routine developed at the NASA Goddard Cumulus Ensemble Modeling Group (GCE; Tao et al. 2003). For liquid-water clouds and hail, COT in the visible region is parameterized based on Sui et al. (1998) assuming spherical droplets:

$$\tau_x = 1.5 \times \int \frac{q_x}{R_{ex}} dz \,, \qquad (4)$$

where the subscript x denotes the hydrometeor specie (cloud water, rain or graupel) and R_{ex} is its respective effective radius. Effective radii are derived from the respective microphysical

formulations as the ratio of the second to the third moment of the size distributions. For those species represented by a negative exponential size distribution this yields:

$$R_{ex} = \frac{1}{2}\left(\frac{q_x}{a_{mx}N_x}\right)^{1/b_{mx}}, \qquad (5)$$

where the constants a_{mx} and b_{mx} are the m-D constants used in equation 2, which are listed in Table 1 for each specie and each scheme. For cloud ice and snow, COT is parameterized based on a formula derived for cirrus ice-crystals by Fu and Liou (1993):

$$\tau_x = \int 10^4 \times (q_x) \times \left(0.006656 + \frac{3.686 \times 10^{-4}}{R_{ex}}\right) dz, \qquad (6)$$

The effective radii are also defined as the ratio of the 2nd to the 3rd moment (equation 5). Note that THOM assumes a combined exponential and gamma distribution for the snow specie and relates the third moment of its distribution to the second moment using empirical relations derived by Field et al. (2005). The relations summarized in their Table 2 are used to determine the second and third moment and hence the effective snow radius for THOM. The empirical coefficients in equation 6 are obtained from Fu and Liou (1993) by fitting scattering calculations to observed snow size distribution data. Total COT is the sum of all species described in equations 4 and 6.

The use of the above outlined GCE method for the calculation of COT might seem inconsistent with the use of the Dudhia (1989) scheme to calculate the shortwave radiative transfer in the simulations. However, the above method was found to be more consistent with the microphysics parameterizations employed (which is the primary focus of this paper), as the Dudhia (1989) scheme bases its calculation of COT on simple empirical relations that, for instance, do not explicly account for variations in particle effective radii and hence are inconsistent with the size distribution assumptions in the diffferent microphysics schemes. As

our main interest was to understand the role of microphysics on deep convective cloud properties, the COT calculation according to GCE was found perferable over the Dudhia (1989) derived COT. (Note that the GCE scheme outlined above is more advanced than the GCE option available in WRF). Moreover, this approach allows for a fair evaluation of simulated against observed cloud properties. As the satellite cannot discriminate between values above 128, all simulated values higher than this value were set to 128.

WRF-simulated CTP is defined as the pressure at the effective emission height of the cloud, which is computed as the level where the integrated longwave absorption COT (from the model top downwards) reaches a value of one (Luo et al. 2010; Van Weverberg et al. 2012b). For consistency with this value, shortwave COT > 2 has been considered in the satellite and model analyses (since shortwave extinction COT is about double the mid-infrared absorption COT). The value of this threshold is somewhat arbitrary, but the same value is applied consistently to the satellite and model fields. A lower value would detect more cloud occurrence in both fields, but retrieved COT at lower values becomes more uncertain because of increased complications presented by the variable land-surface albedo and the increased chance of misinterpreting multi-layered clouds (i.e., thin cirrus overlying low-level cloud). A sensitivity study using a shortwave COT threshold of one changes the cloud occurrences but not the overall quality of the model-satellite agreement.

2.3.2 Observed and simulated Mesoscale Convective System identification

To not only evaluate domain-averaged cloud property statistics, but also obtain information on how well the structure of convective clouds and their anvils are represented in the various

simulations, a cloud-identification and tracking algorithm (Boer and Ramanathan 1997) was applied to the observations and simulations. This method uses TOA narrowband (11 μm) infrared brightness temperatures (BT). The simulated top-of-model (50 hPa) broadband outgoing longwave radiation (OLR) is translated into TOA narrowband BT using regression coefficients computed off-line using the MODTRAN-v4 multiple-scattering radiative transfer algorithm (Anderson et al. 2001). The computations convert the OLR flux into a narrowband 11-μm flux, translate this flux from the model top (50 hPa) to the TOA (0 hPa), and then convert the TOA narrowband flux into a radiance from which the equivalent brightness temperature (BT) is determined. After applying a cloudy and clear-sky classification, the algorithm identifies clouds based on a detection and spread (DAS) cloud identification (Boer and Ramanathan 1997). Individual clouds are assumed to be distinct systems provided that their cold BT cores are separated by warmer BT regions. Our primary focus is the detection of MCSs, which are defined following Laing and Fritsch (1993). Each MCS must have a core with a BT less than 219 K and an area larger than 50,000 km^2. Further, each core must be surrounded by an anvil-cloud with a BT less than 240 K and the combined size of the MCS (core and anvil) must exceed 100,000 km^2. In the following analysis, properties of the cores and anvils of MCSs have been analyzed according to the definitions above, except that the anvils include all MCS clouds that do not belong to the MCS core region (including clouds warmer than 240 K). MCS-tracking has been performed for identical domains in the model and the observations (17° N to 20° S and 100° E to 162° E). However, as observed cloud-property data (COT and CTP) were only available for the slightly eastward domain, shown in Figure 1, all statistics in the following sections are for the area common between the model and the observed cloud properties domains, further referred to as analysis domain (Fig. 1).

3. Results

3.1 ISCCP Cloud Classification

As an example, Figure 3 shows a representative snapshot of the spatial distribution of the different cloud classes according to the ISCCP classification, based on satellite retrieved and simulated COT and CTP distributions in the observations and the three experiments. A 6-day average of the area covered by all of the nine ISCCP cloud classes in the observations and all experiments is provided in Figure 4. More cloud-cover statistics are given in Table 2. In the observations, high clouds dominate by covering 45% of the analysis domain (Table 2) and account for over 80% of the total cloud-cover, which is largely attributable to cirrostratus clouds (Fig. 4). Consistent with previous studies (Blossey et al. 2007, Zhou et al. 2007), all three microphysics schemes underestimate cirrus and cirrostratus cloud-cover. The largest underestimation of high clouds occurs in WSM6 (Fig. 4 and Table 2), while it simulates more low-level optically thick clouds compared to the observations. A similar picture can be drawn for MORR, where high cloud-cover is underestimated and low cloud-cover overestimated.

Caution should be taken when interpreting the low cloud-cover, as the more extended high clouds in the observations might be hiding low clouds underneath. Indeed, the classification employed here cannot discriminate between multilayer clouds. However, since cloud-top height in the model was determined based on IR COT, similar to how the satellite determines cloud tops, the model and observations would be affected equally by this limitation. Therefore, this limitation is not expected to influence the model-observation comparison, but it should be

understood that this method will likely underestimate the occurrence of low clouds when high clouds are present.

Consistent with Wang et al. (2009), many more high clouds are simulated by the THOM experiment. While THOM improves the distribution over high, middle and low clouds (Table 2), it also has a tendency to overestimate the optical thickness distribution. Hence, despite an improvement compared to WSM6 and MORR, there is still a significant underestimation in the cirrus and cirrostratus cover, while a large overestimation occurs of the clouds categorized as cumulonimbus (Fig. 4). Total cloud-cover is considerably improved by THOM, compared to WSM6 and MORR (Table 2).

The question arises to what extent these differences in cloud classes are associated with deep convection by MCSs. Using the MCS identification classification of Boer and Ramanathan (1997), the hatched areas on Figure 4 show the area of each cloud class that is identified as being part of an MCS. About half of the high clouds in the observations appear to be associated with an MCS for this 6-day period (Fig. 4 and Table 2), which is consistent with the observations by Luo and Rossow (2004), based on 18 years of satellite data. From Figure 4, MCS-related cirrus and cirrostratus exhibit a significant underestimation in WSM6 and MORR, while THOM is able to closely capture those thinner high clouds. However, THOM overestimates the area covered by MCS-cumulonimbus clouds (Fig. 4). While not a primary focus of our study, it is remarkable that thin, high non-MCS related clouds (the unhatched regions in Fig. 4) exhibit very limited sensitivity to microphysics.

3.2 MCS statistics

Using the cloud identification and tracking algorithm described in section 2.3.2, MCSs were identified in the observations and the three model experiments. Statistics on the MCS properties are provided in Table 3 and visualized in Figure 5. MCS anvils and core regions are defined according to the Laing and Fritsch (1993) definitions based on brightness temperatures, as mentioned in section 2.3.2. Again, WSM6 and MORR behave similarly and both slightly underestimate the individual MCS sizes (Fig. 5 and Table 3). More remarkable is that both schemes only produce half the amount of observed MCS tracks (Table 3). The significant underestimation of MCS-related clouds in these schemes (Figure 4) is hence due to both too small MCSs and too few MCSs present. The proportion of core versus anvil is thus well captured (Fig. 5). THOM, however, closely captures the number of observed MCS tracks, but the sizes of individual MCSs are too large compared to observations. The enlarged MCS sizes are mainly due to excessive core sizes (Fig. 5). This is consistent with Figure 4, showing an overestimation of the MCS-cumulonimbus clouds, while the MCS-cirrus and -cirrostratus cloud-cover is better captured.

From Table 3, all simulations produce too low brightness temperatures in the anvils, while BT is better captured in the core regions. Previous research (Li et al. 2008, Matsui et al. 2009, Varble et al. 2011) often reported significant underestimations of BT. Further, all of the simulations produce clouds that are optically too thick, mainly within the anvils (Table 3). The latter seems to be consistent with excessive radar reflectivities found in many other CRM studies in the TWP (Blossey et al. 2007, Li et al. 2008, Varble et al. 2011) and explains the low anvil BTs. The differences between the different microphysics schemes are smaller than the differences between the simulations and the observations.

3.3 MCS dynamics

Microphysics can affect the MCS properties for instance through the release of latent heat that modulates the MCS dynamics. To assess whether the more numerous MCS-tracks and the larger MCSs in THOM (discussed above) are indeed related to such dynamical influences, the average updraft properties for the analysis domain and for the MCS cores are shown in Figure 6 for all experiments. THOM has a larger total updraft mass-flux associated with its MCSs than WSM6 and MORR (Fig. 6a), but when viewed over the analysis domain the total updraft mass-flux in all schemes is very similar (Fig. 6c). Further, the mean updraft speeds are remarkably similar among the three schemes (Fig. 6b and d). This is consistent with Wu et al. (2009), who found updraft strengths to be very similar whether THOM or WSM6 was employed during the active monsoon season in the TWP. Figure 7 provides more details on how the updrafts are organized within each of the simulations since. Again, all three schemes seem to behave very similarly. The number of updrafts (Fig. 7b), their individual sizes (Fig. 7c) and their mean updraft speeds (Fig. 6d) are not significantly different between the experiments, which leads to the very similar domain-total updraft mass-fluxes (Fig. 6c). This suggests that differences in the properties and organization of updrafts seem to play a minor role in the very different properties of MCSs between the different schemes. This points to a potentially more important role of the microphysical processes themselves, as is discussed next.

3.4 MCS microphysics

3.4.1 Vertical profiles

A second possible impact that microphysics can have on deep convection, besides on the dynamics, is more directly related to the microphysical processes. Differences in particle size distributions, for instance, can modulate the particle fall speeds or the rate of processes like deposition and sublimation. Vertical profiles of hydrometeor mixing ratio, number concentration, particle diameter and vertical fall velocities for all frozen species are provided in Figures 8-10 (cloud water profiles of all schemes are similar and not shown). The profiles are averaged over those grid cells associated only with MCS cores for all three experiments.

The three microphysics schemes produce very different vertical profiles of q_I (Fig. 8a), which is much larger across the troposphere in WSM6, compared to MORR and THOM, consistent with e.g. Wang et al. (2009). Even more remarkable is the very large mean cloud-ice diameter (Fig. 8c) and fall speed in WSM6 (Fig. 8d), which are much larger than usually observed for cloud-ice particles (e.g. Lawson et al. 2006, Heymsfield et al. 2007). MORR and THOM include a size threshold for cloud ice and the portion of the cloud-ice size distribution that is larger than this threshold is automatically transferred to the snow specie. WSM6 does not include such a threshold, which is the likely reason for its large q_I. Also, recall that WSM6 is the only scheme that does not explicitly predict N_I (Table 1), but diagnoses N_I from q_I. This is unlike many other one-moment microphysics schemes that diagnose N_I from temperature (e.g. Lin et al. 1983, Rutledge and Hobbs 1984). Apparently, the relation used in WSM6 produces very small N_I aloft (Fig. 8b; note the logarithmic scale) and hence very large particles that fall out more quickly compared to MORR and THOM.

More similarities between the microphysics schemes exist as far as the snow specie is concerned (Fig. 9). The vertical profiles of q_X (Fig. 9a) above the melting layer (about 5 km) are

indeed dominated by snow in all three schemes. Snow content is somewhat lower in WSM6, due to the absence of the size threshold for cloud ice as outlined above. THOM has more snow in the upper troposphere, which is related to the large N_S (Fig. 9b) and small fall velocities (Fig. 9d) at these altitudes (note the logarithmic scale in Figure 9b). However, MORR has more snow in the middle troposphere (Fig. 9a). Also note that the snow fall velocities there are generally faster in MORR compared to the other two schemes (Fig. 9d). MORR is the only scheme that explicitly predicts N_S, which apparently leads to fewer snowflakes in the middle troposphere, larger snow diameters and hence somewhat quicker fallout.

The q_G between WSM6 and MORR are similar (Fig. 10a), although the two-moment MORR scheme has smaller graupel particles (Fig. 10c). THOM, however, produces remarkably small q_G (Fig. 10a). The most likely reason for this is that THOM is the only scheme that has a rather rigid conversion of rimed snow into graupel. Only when the riming growth of snow exceeds five times its depositional growth will a portion of the rimed snow be converted to graupel. WSM6 and MORR, however, only require that significant q_S and q_C for snow to be partially transferred to the graupel species. The smaller q_G and the larger q_S in the Thompson scheme compared to the WSM6 scheme are consistent with findings by Wang et al. (2009).

3.4.2 Implications for MCS properties

The main feature emerging from the analysis of the vertical hydrometeor profiles in the previous section is that THOM seems to be dominated by slower falling hydrometeor species compared to WSM6 and MORR, mainly in the upper troposphere. Indeed, snow – the dominant specie aloft in all schemes – falls considerably slower in THOM compared to the other schemes.

Further, cloud ice falls slower too, and the fastest specie – graupel – is virtually non-existent in THOM, while abundant in the other schemes. The slow fallout of snow in the upper troposphere is demonstrated by Figure 11, which relates q_S to the fall speed for each of the schemes for altitudes above 10 km. From this figure, snow falls about half as fast in THOM compared to the other schemes for any q_S. Recall from Figure 2 that this is not due to differences in the fall speed-diameter relation applied in THOM; so the difference must be attributed to THOM having larger N_S of smaller snowflakes compared to the other two schemes (Fig. 9b and c).

While MORR explicitly predicts N_S, it has to be diagnosed in one-moment schemes, such as WSM6 and THOM. WSM6 represents the snow size distribution by an exponential function and, hence, N_S can be diagnosed from λ_S and N_{0S} following:

$$N_S = \frac{N_{0S}}{\lambda_S}, \qquad (7)$$

where N_{0S} is provided in Table 1 and λ_S is given by equation 2. THOM, however, has a combined exponential and gamma snow size distribution (Table 1) and, hence, diagnoses N_S from empirical relations derived by Field et al. (2005) as follows:

$$N_S = a(T_c) \times \left(\frac{\rho q_S}{a_{ms}} \right)^{b(T_c)}, \qquad (8)$$

where the coefficient $a(T_c)$ and exponent $b(T_c)$ are polynomial functions of temperature T_c (given in Table 2 in Field et al. 2005) and a_{ms} is provided in Table 1. The relations by Field et al. (2005) were derived for mid-latitude stratiform clouds with temperatures ranging from -55°C to 0°C and at the very low temperatures (< -80°C) near the tropopause apparently yield N_S that are a couple orders of magnitude larger than for the other schemes. As the snow diameter, D_S, is dependent on N_S, this also yields smaller snow particles (Fig. 9c), which will fall much more

slowly (Fig. 2). Consequently, the average downward precipitation flux aloft will be smaller in THOM compared the other two schemes, which – provided similar production rates – yields a larger buildup of condensate in the upper troposphere.

Figure 12 shows vertical cross sections through the MCSs, depicted in Figure 3, and provides further insight into the simulated MCS structure. The left-hand panels represent the dynamic features of the average MCSs, showing the in- and outflow strength (colors and arrows), as well as the vertical velocities of snow (contours). Again, this figure features the very small sedimentation velocities of snow aloft in THOM compared to the other schemes. Obviously, this leads to a larger buildup of condensate and this condensate (mainly snow) has nowhere to go but be lofted to the tropopause outflow of the MCS. Also notice that the outflow strengths are very similar between the three schemes. Snow is hence transported over large distances from the main updraft cores in THOM. In WSM6 and MORR, however, the quicker fallout of snowflakes prevents the snow mass from being transported over such large distances.

The right-hand panels in Figure 12 show cross sections of the extinction coefficient as well as the relative humidity with respect to ice for each experiment. Clouds spread out against the tropopause much farther in THOM. These high clouds, consisting of larger snow masses and smaller effective radii also have larger extinction coefficients compared to the other schemes. Recall that MCSs are defined based on BT and it is plausible that the (physically and optically) thicker high clouds in THOM lead to excessive areas of low BT and hence produce larger MCS cores compared to the other schemes (Table 3). Eventually this will not only lead to larger MCSs, but also to a larger number of convective systems that reach the size threshold to be identified as an MCS.

3.4.3 Implications for MCS upper tropospheric humidity levels

The right-hand panels on Figure 12 indicate that the larger upper tropospheric cloud extent in THOM is associated with moister upper levels. As the outflow intensity in this scheme is comparable to the other schemes (that have drier upper tropospheres), this must be related to the sublimation of snow, which returns significant portions of the condensate back to the vapor phase. A debate is ongoing concerning whether the often observed elevated-moisture plume downwind from MCSs should be mainly attributed to sublimation of ice, or by vapor advection from the updraft core regions (Soden 2004, Luo and Rossow 2004, Wright et al. 2009). Our analysis shows that – at least within this CRM – vapor is most likely originating from sublimation of ice, consistent with Wright et al. (2009). While all schemes have similar upper-air outflow dynamics, the scheme that produces the slowest falling snow and largest snow mass aloft (and hence the most sublimation) eventually produces a moister upper troposphere.

3.5 MCS surface precipitation

The above-described influence of microphysics parameterization on the formation of clouds may impact the fallout of condensate at lower levels and surface precipitation. Figure 13 and Table 4 summarize the main features of accumulated surface precipitation. MORR produces about 15% and 25% less mean surface precipitation compared to WSM6 and THOM respectively (Table 4). This is a considerable difference provided the extent of the domain and the 6-day simulation time. Since the domain-total updraft mass-flux and updraft strength is very similar among the several schemes (section 3.2.2), the difference in surface precipitation likely

reflects differences in precipitation efficiency, which is largely controlled by sublimation and evaporation of precipitation. The cooling associated with these processes ultimately causes downdrafts and, hence, differences in downdraft size and strength would parallel the differences in the evaporation and sublimation among the experiments.

Downdraft characteristics of the three experiments are given in Figure 14. MORR has the largest downdraft mass flux and strongest downdraft velocities in the lower troposphere, while THOM has the largest downdraft mass flux in the upper troposphere (consistent with previous analysis showing that more snow sublimation occurs near the tropopause). In the lower troposphere, where the largest differences in downdraft mass flux between MORR and the other two schemes occur, rain is the only species that remains. Those differences thus likely reflect differences in rain evaporative cooling.

The precipitation efficiency in CRMs can be very sensitive to rain evaporation rates (e.g. Morrison and Milbrandt 2011), which are largely controlled by the rain drop size (Van Weverberg et al. 2012a). Size-distribution characteristics of precipitation within the downdrafts are depicted in Figure 15, which shows averages only for vertical columns that experience significant surface precipitation rates. MORR has smaller rain drops throughout most of the lower troposphere, while THOM is associated with larger raindrops (Fig. 15b). A particular feature of two-moment schemes, such as MORR, is that the N_R reflects the N_X of the frozen condensate from which it originates. Therefore, the small snow and graupel particles in MORR (Fig. 15d and f) melt into small rain drops. In one-moment schemes, such as THOM and WSM6, N_R is diagnosed and there is no memory of the size distribution characteristics of the frozen specie from which the rain originated. It should be noted that THOM attempts to circumvent this limitation by diagnostically adapting the rain mass-weighted mean size according to the mass-

weighted sizes of snow and graupel and, hence, is able to mimic features of two-moment schemes. However, due to the larger sizes of snow and graupel near the melting layer, raindrops are still larger compared to MORR. Thus, it seems likely that differences in rain evaporation play a significant role in the surface precipitation sensitivity to the microphysical parameterizations applied. More complex two-moment schemes, such as MORR, explicitly treat processes such as size sorting, which in this case yields smaller drops, more evaporation, and smaller surface precipitation.

An estimate of the observed surface precipitation accumulation for the model domain and simulation period was obtained from the Global Precipitation Climatology Project (GPCP; Adler et al. 2003), established by the World Climate Research Program. GPCP provides daily global surface precipitation data on a 1° resolution. While Figure 13 and Table 4 show that the surface precipitation produced by MORR is somewhat closer to the observed precipitation, they mainly show that all of the simulations largely overestimate the surface precipitation, even considering the relative negative bias error of about 10 to 15% in the observed GPCP precipitation in the TWP (Adler et al. 2012). The location of the intense precipitation corridor north of Papua New Guinea is reasonably well captured, while a dry bias exists in all simulations across northern Australia. This could in part be associated with a wet bias in the GPCP observed precipitation in northern Australia in southern hemispheric summer (Adler et al. 2012).

Reasons for the general overestimation of surface precipitation might not be associated with the microphysics parameterization. Recall that the grid spacing used in our simulation might still be too coarse to fully resolve convective updrafts. Indeed, observational studies of convective updrafts over tropical oceans (Lucas et al. 1994, Anderson et al. 2005, Heymsfield et al. 2010) typically report updraft diameters that are smaller than 4 km. Updrafts in our simulations were

generally much wider than observed (Fig. 7a), consistent with Deng and Stauffer (2006), and which likely results in too much upward mass transport. Also, Bryan and Morrison (2012) report that detrainment of clouds is very dependent on the model resolution. They found surface precipitation to be up to 30% lower using a 250 m grid spacing compared to simulations using a 4-km grid spacing, due to the larger detrainment rates. Varble et al. (2011) found smaller (but still important) surface precipitation overestimations over the TWP using a suite of CRMs with higher resolution (± 1 km). Too much upward mass transport and a lack of detrainment in our simulations might play an important role in the overestimated surface precipitation and optical thickness.

4. Summary and discussion

Progress in the representation of convection-associated cloud structures within cloud-resolving models can only be achieved if the physical reasons for discrepancies between different models are truly understood. This paper presents a detailed analysis of convection-permitting simulations that is aimed at increasing the understanding of the role of parameterized cloud microphysics in the simulation of MCSs in the tropical western pacific. Simulations with three commonly used bulk microphysics parameterizations with varying complexity have been evaluated against satellite-retrieved cloud properties. An MCS identification algorithm was applied to the observations and the simulations to evaluate the properties of individual cloud systems. Different from many previous studies, these individual cloud systems could be tracked over large distances due to the very large domain employed.

The analysis demonstrates that the simulation of MCSs is very sensitive to the parameterization of microphysical processes. The most crucial element was found to be the fall velocity of frozen condensate in the upper troposphere. Microphysics schemes that have slow sedimentation rates of ice aloft experience a larger buildup of condensate. This condensate is picked up by the updraft outflow near the tropopause and only gradually sublimates; so anvils in these systems extend much farther from the updraft cores compared to schemes that have a faster fallout of ice. The scheme with the slowest fallout speed (THOM) simulated the observed number of MCSs, while in the schemes with faster fallout simulated only half as many systems (WSM6, MORR). However, the buildup of condensate aloft in the scheme with slow fallout (THOM) seemed to be excessive, such that the MCSs were too large, too optically thick, and had core regions that were too large. Elevated levels of relative humidity in the upper troposphere, downwind from MCSs, seemed to predominantly originate from ice sublimation rather than from vapor advection, supporting findings by Wright et al. (2009).

Surface precipitation was found to be rather insensitive to the microphysics parameterization, although two-moment schemes better-capture the size sorting effects within the MCSs and experience more evaporation, thereby reducing surface precipitation by about 20% compared to the other schemes. Nevertheless, all simulations significantly overestimated surface precipitation. Along with overestimated convective cloud optical thickness, this suggests that updraft mass fluxes in all simulations were excessively large. Some studies suggest that, for the 4-km spatial resolution employed here, updrafts are forced on larger-than-natural scales (Deng and Stauffer 2006) and clouds experience a lack of detrainment (Bryan and Morrison 2012), which might explain at least part of the overestimated surface precipitation. Observations of updraft mass

fluxes from radar would be most helpful to improve our understanding of the impact of horizontal grid spacing on updraft properties.

In our simulations, the more complex two-moment schemes did not have superior performances to the simpler one-moment schemes. The slower fall velocities in the (one-moment) scheme (THOM) with more realistic anvils and the correct number of MCSs were found to be due to the large number concentration aloft of snowflakes (rather than different velocity-diameter relations. Hence, to better capture the representation of high tropical clouds, more attention should be given to the processes that influence snow and ice number concentrations, such as nucleation of ice-crystals and the subsequent aggregation to larger snowflakes, whether based on empirical relations in one-moment schemes or a better representation of ice nucleation processes within two-moment schemes. Better observations of microphysical properties (mainly of ice particle size distributions) of tropical anvil-clouds are highly needed to develop such improved parameterizations.

It should be stressed that the study presented here focused on clouds associated with MCSs. The non-convective high cloud-cover was underestimated in all simulations (Fig. 4) and exhibited very limited sensitivity to microphysics. Recent observations suggest that such non-convective high and thin clouds might be related to the frequent occurrence of very large super-saturations (Spichtinger et al. 2003, Jensen et al. 2005, Kramer et al. 2009), which were not present in our simulations. A proper representation of such thin clouds might be contingent on a better representation of the upper model boundary, such as higher vertical resolution and a better approach to calculating saturation vapor-pressure. For instance, two of the schemes tested in our study impose a lower bound of 193 K on temperature for the calculation of saturation vapor-

pressure, while temperature near the cloud tops frequently dropped below this value. Future studies should take this aspect into account.

Further, our study focused on the impact of microphysics on convective clouds and did not study any radiative feedbacks associated with these clouds. While such feedbacks usually play a secondary role on the short time-scales in our study (e.g. Wang et al. 2009), the different cloud and hydrometeor properties among the schemes suggest that they should not be ignored on longer time-scales. In order to study such radiative feedback, better coupling of the parameterization of microphysical processes and radiative processes is indispensable.

5. Acknowledgements

Research by Van Weverberg, Vogelmann, Lin, Luke, Cialella and Jensen was supported by the Laboratory Directed Research and Development Program at Brookhaven National Laboratory, the U.S. Department of Energy's Atmospheric Science Program Atmospheric System Research (ASR), an Office of Science Office of Biological and Environmental Research program, under contract DE-AC02-98CH10886, and by the Earth System Modeling Program via the FASTER project (www.bnl.gov/esm). M. Khaiyer and P. Minnis were also supported by the ASR under Inter agency Agreement, DE-SC0000991/003. We kindly acknowledge the use of the NY Blue, a Blue Gene/L supercomputer that was used for the WRF simulations.

6. References

Ackerman, T. P., K. N. Liou, F. P. J. Valero, and L. Pfister, 1988: Heating rates in tropical anvils. *J. Atmos. Sci*., **45**, 1606-1623.

Adler, R.F., G.J. Huffman, A. Chang, R. Ferraro, P.-P. Xie, J. Janowiak, B. Rudolf, U. Schneider, S. Curtis, D. Bolvin, A. Gruber, J. Susskind, P. Arkin, E. Nelkin, 2003: The Version-2 Global Precipitation Climatology Project (GPCP) monthly precipitation analysis (1979-present). *J. Hydrometeor*., **64**, 1147-1167.

———, G. Gu, G.J. Huffman, 2012: Estimating climatological bias errors for the Global Precipitation Climatology Project (GPCP). *J. Appl. Meteor*., **51**, 84-99.

Anderson, N.F., C.A. Grainger, J.L. Stith, 2005: Characteristics of strong updrafts in precipitation systems over the central tropical Pacific Ocean and in the Amazon. *J. Appl. Meteor.*, **44**, 731-738.

Anderson, G. P., A. Berk, P. K. Acharya, M. W. Matthew, L. S. Bernstein, J. H. Chetwynd, H. Dothe, S. M. Adler-Golden, A. J. Ratkowski, G. W. Felde, J. A. Gardner, M. L. Hoke, S. C. Richtsmeier, and L. S. Jeong, 2001: MODTRAN4, version 2: Radiative transfer modeling. *SPIE-Int. Soc. Opt. Eng.*, **4381**, 455– 459.

Benedict, J.J., D.A. Randall, 2009: Structure of the Madden-Julian Oscillation in the superparameterized CAM. *J. Atmos. Sci*., **66**, 3277-3296.

Blossey, P.N., C.S. Bretherton, J. Cetrone, M. Kharoutdinov, 2007: Cloud-resolving model simulations of KWAJEX: Model sensitivities and comparisons with satellite and radar observations. *J. Atmos. Sci*., **64**, 1488-1508.

Boer, E.R., V. Ramanathan, 1997: Lagrangian approach for deriving cloud characteristics from satellite observations and its implications to cloud parameterization. *J. Geophys. Res*., **102**, 21383-21399.

Bryan, G.H., H. Morrison, 2012: Sensitivity of a simulated squall line to horizontal resolution and parameterization of microphysics. *Mon. Wea. Rev*., in press.

Cox. G.P., 1988: Modelling precipitation in frontal rainbands. *Quart. J. Roy. Meteor. Soc.,* **114**, 115-127.

Del Genio, A. D., and J. Wu, 2010: The Role of Entrainment in the Diurnal Cycle of Continental Convection. *J. Climate*, **23**, 2722–2738.

———, 2011: Representing the sensitivity of convective cloud systems to tropospheric humidity in general circulation models. *Surv. Geophys*., doi: 10.1007/s10712-0119148-9

Deng, A., Stauffer, D. R., 2006: On improving 4-km mesoscale model simulations. *J. Appl. Meteorol. and Climatology*, **45**, 361-381.

Dudhia, J., 1989: Numerical study of convection observed during the winter monsoon experiment using a mesoscale two-dimensional model. *J. Atmos. Sci*., **46**, 3077-3107.

Ferrier, B. S., 1994: A double-moment multiple-phase four-class bulk ice scheme, Part I: description. *J. Atmos. Sci.*, **51**, 249-280.

———, W.-K. Tao, J. Simpson, 1995: A double-moment multiple-phase four-class bulk ice scheme. Part II: Simulations of convective storms in different large-scale environments and comparison with other bulk parameterizations. *J. Atmos. Sci*., **52**, 1001-1033.

Field, P. R., R. J. Hogan, P. R. A. Brown, A. J. Illingworth, T. W. Choularton, R. J. Cotton, 2005: Parameterization of ice-particle size distributions for mid-latitude stratiform cloud. *Quart. J. Roy. Meteor. Soc.*, **131**, 1997-2017.

Fu, Q., K.-N. Liou, 1993: Parameterization of the radiative properties of cirrus clouds. *J. Atmos. Sci*., **50**, 2008–2025.

Grabowski, W.W., 2000: Cloud microphysics and the tropical climate: Cloud-resolving model perspective. *J. Climate*, **13**, 2306-2322.

Heymsfield, A. J., M. Kajikawa, 1987: An improved approach to calculating terminal velocities of plate-like crystals and graupel. *J. Atmos. Sci*., **44**, 1088-1099.

———, G.-J. van Zadelhoff, D.P. Donovan, F. Fabry, R.J. Hogan, A.J. Illingworth, 2007: Refinements to ice particle mass dimensional and terminal velocity relationships for ice clouds. Part II: Evaluation and parameterizations of ensemble ice particle sedimentation velocities. *J. Atmos. Sci*., **64**, 1068-1088.

Heymsfield, G.M., L. Tian, A.J. Heymsfield, L. Li, S. Guimond, 2010: Characteristics of deep tropical and subtropical convection from nadir-viewing high-altitude airborne Doppler radar. *J. Atmos. Sci*., **67**, 285-308.

Hong, S.-Y., J.-O. Jade Lim, 2006: The WRF single-moment 6-class microphysics scheme (WSM6). *J. Korean Meteor. Soc*., **42**, 129-151.

Houze, R.A., P.V. Hobbs, P.H. Herzegh, D.B. Parsons, 1979: Size distributions of precipitation particles in frontal clouds. *J. Atmos. Sci*., **36**, 156-162.

Jensen, E.J., D. Starr, O. Toon, 2004: Mission investigates tropical cirrus clouds. Eos, 85, 45-50.

———, J.B. Smith, L. Pfister, J.V. Pittman, E.M. Weinstock, D.S. Sayres, R.L. Herman, R.F. Troy, K. Rosenlof, T.L. Thompson, A.M. Fridlind, P.K. Hudson, D.J. Cziczo, A.J.

Heymsfield, C. Schmitt, J.C. Wilson, 2005: Ice supersaturation exceeding 100% at the cold tropical tropopause: Implications for cirrus formation and dehydration. *Atmos. Chem. Phys*., **5**, 851-862.

Kain, J. S., J. M. Fritsch, 1993: Convective parameterization for mesoscale models: The Kain-Fritsch scheme. The Representation of Cumulus Convection in Numerical Models. *Meteorol. Monogr.*, **24**, 165-170.

Kalnay, E., M. Kanamitsu, W.E. Baker, 1990: Global numerical weather prediction at the National-Meteorological Center. *Bull. Amer. Meteor. Soc*., **71**, 1410-1428.

Khairoutdinov, M. F., and D.A. Randall, 2001: A cloud resolving model as a cloud parameterization in the NCAR Community Climate System Model: Preliminary Results. *Geophys. Res. Lett*., **28**, 3617-3620

Kramer, M., C. Schiller, A. Afchine, R. Bauer, I. Gensch, A. Mangold, S. Schlicht, N. Spelten, N. Sitnikov, S. Bormann, M. de Reus, P. Spichtinger, 2009: Ice supersaturation and cirrus cloud crystal numbers. *Atmos. Chem. Phys*., **9**, 3505-3522.

Laing, A.G., J.M. Fritsch, 1993: Mesoscale convective systems over the Indian monsoon region. *J. Climate*, **6**, 911-919.

Lawson, R.P., B. Baker, B. Pilson, Q. Mo, 2006: In situ observations of the microphysical properties of wave, cirrus and anvil clouds. Part II: Cirrus clouds. *J. Atmos. Sci*., **63**, 3186-3203.

Li, Y., E.J. Zipser, S.K. Krueger, M. A. Zulauf, 2008: Cloud-resolving modelling of deep convection during KWAJEX. Part I: Comparison to TRMM satellite and ground-based radar observations. *Mon. Wea. Rev*., **136**, 2699-2712.

Liang, X.Z., X.Q. Wu, 2005: Evaluation of a GCM subgrid cloud-radiation interaction using cloud-resolving model simulations. *Geophys. Res. Lett*., **32**, doi: 10.1029/2004GL022301

Lin, Y.- L., Farley, R. D., H. D. Orville, 1983: Bulk parameterization of the snow field in a cloud model. *J. Clim. Appl. Meteorol.*, **22**, 1065-1092.

Liu, J. Y., H. D. Orville, 1969: Numerical modeling of precipitation and cloud shadow effects on mountain-induced cumuli. *J. Atmos. Sci*., **26**, 1283-1298.

Locatelli, J. D., P. V. Hobbs, 1974: Fall speeds and masses of solid precipitation particles. *J. Geophys. Res*., **79**, 2185-2197.

Lucas, C., E.J. Zipser, M.A. Lemone, 1994: Vertical velocity in oceanic convection off tropical Australia*. J. Atmos. Sci*., **51**, 3183-3193.

Luo, Z., W.B. Rossow, 2004: Characterizing tropical cirrus life cycle, evolution, and interaction with upper-tropospheric water vapour using lagrangian trajectory analysis of satellite observations*. J. Climate*, **17**, 4541-4563.

Luo, Z. J., G. Y. Liu, and G. L. Stephens. 2010: Use of A□Train data to estimate convective buoyancy and entrainment rate. *Geophys. Res. Lett.,* **37**, L09804, doi:10.1029/2010GL042904.

Mace, G.G., M. Deng, B. Soden, E. Zipser, 2006: Association of tropical cirrus in the 10-15 km layer with deep convective sources: An observational study combining millimeter radar data and satellite-derived trajectories*. J. Atmos. Sci.*, **63**, 480-503.

Matsui, T., X. Zeng, W.- K. Tao, H. Masunaga, W. S. Olson, S. Lang, 2009: Evaluation of long-term cloud-resolving model simulations using satellite radiance observations and multifrequency satellite simulators. *J. Atmos. Ocean. Tech.*, **26**, 1261-1274.

May, P.T., J.H. Mather, G. Vaughan, C. Jakob, G.M. McFarquhar, K.N. Bowen, G.G. Mace, 2008: The tropical warm pool international cloud experiment. *Bull. Amer. Meteor. Soc*., 89, 629-645.

Minnis, P., L. Nguyen, R. Palikonda, P. W. Heck, D. A. Spangenberg, D. R. Doelling, J. K. Ayers, W. L. Smith, Jr., M. M. Khaiyer, Q. Z. Trepte, L. A. Avey, F.-L. Chang, C. R. Yost, T. L. Chee, and S. Sun-Mack, 2008: Near-real time cloud retrievals from operational and research meteorological satellites. *Proc. SPIE Europe Remote Sens. 2008, Cardiff, Wales*, UK, 15-18 September, **7107-2**, 8 pp.

———, S. Sun-Mack, D. F. Young, P. W. Heck, D. P. Garber, Y. Chen, D. A. Spangenberg, R. F. Arduini, Q. Z. Trepte, W. L. Smith, Jr., J. K. Ayers, S. C. Gibson, W. F. Miller, V. Chakrapani, Y. Takano, K.-N. Liou, Y. Xie, and P. Yang, 2011: CERES Edition-2 cloud property retrievals using TRMM VIRS and Terra and Aqua MODIS data, Part I: Algorithms. *IEEE Trans. Geosci. Remote Sens*., **49**, 11, 4374-4400.

Mlawer, E.J., S.J. Taubman, P.D. Brown, M. J. Iacono, S.A. Clough, 1997: Radiative transfer for inhomogeneous atmospheres: RRTM, a validated correlated-k model for the longwave. *J. Geophys. Res*., **102**, 16663-16682.

Morrison, H., G. Thompson, V. Tatarskii, 2009: Impact of cloud microphysics on the development of trailing stratiform precipitation in a simulated squall line: Comparison of one- and two-moment schemes. *Mon. Wea. Rev*., **137**, 991-1007.

———, J.A. Milbrandt, 2011: Comparison of two-moment bulk microphysics schemes in idealized supercell thunderstorm simulations. *Mon. Wea. Rev*., **139**, 1103-1130.

Randall, D., M. Khairoutdinov, A. Arakawa, W. Gabowski, 2003: Breaking the cloud parameterization deadlock. *Bull. Amer. Meteor. Soc*., **84**, 1547-1564.

Reisner, J., Rasmussen, R. M., R. T. Bruintjes, 1998: Explicit forecasting of supercooled liquid water in winter storms using the MM5 mesoscale model. *Quart. J. Roy. Meteor. Soc.*, **124**, 1071-1107.

Rossow, W.B., R.A. Schiffer, 2001: Advances in understanding clouds from ISCCP. *Bull. Amer. Meteor. Soc*., **80**, 2261-2287.

Rutledge, S. A., P. V. Hobbs, 1984: The mesoscale and microscale structure and organization of clouds and precipitation in mid-latitude cyclones. Part XII: A diagnostic modelling study of precipitation development in narrow cold-frontal rainbands. *J. Atmos. Sci*., **41**, 2949-2972.

Schmitt, C.G., A.J. Heymsfield, 2009: The size distribution and mass-weighted terminal velocity of low-latitude tropopause cirrus crystal populations. *J. Atmos. Sci*., **66**, 2013-2028.

Seifert, A., K. D. Beheng, 2001: A double-moment parameterization for simulating autoconversion, accretion and self-collection. *Atmos. Res*., **59-60**, 265-281.

Skamarock, W.C., J.B. Klemp, J. Dudhia, D.O. Gill, D.M. Barker, W. Wang, J.G. Powers, 2007: A description of the Advanced Research WRF Version 2. *NCAR technical note NCAR/TN-468+STR*.

Soden, B.J., 2004: The impact of tropical convection and cirrus on upper tropospheric humidity: A lagrangian analysis of satellite measurements. *Geophys. Res. Lett.*, **31**, doi:10.1029/2004GL020980.

Spichtinger, P., K. Gierens, W. Read, 2003: The global distribution of ice-supersaturated regions as seen by the microwave Limb sounder. *Quart. J. Roy. Meteor. Soc*., **129**, 3391-3410.

Stephens, G.L., 2005: Cloud feedback in the climate system: A critical review. *J. Climate*, **18**, 237-273.

Su, H., S.S. Chen, C.S. Bretherton, 1999: Three-dimensional week-long simulations of TOGA COARE convective systems using the MM5 mesoscale model. *J. Atmos. Sci*., **56**, 2326-2344.

Sui, C. H., X. Li, M.- J. Yang, 2007 : On the definition of precipitation efficiency. *J. Atmos. Sci*., **64**, 4506-4513.

Tao, W.-K., J. Simpson, D. Baker, S. Braun, M.-D. Chou, B. Ferrier, D. Johnson, A. Khain, S. Lang, B. Lynn, C.-L. Shie, D. Starr, C.-H. Sui, Y. Wang, P. Wetzel, 2003: Microphysics, radiation and surface processes in the Goddard Cumulus Ensemble (GCE) model, *Meteorol. Atmos. Phys*., **82**, 97-137.

Thompson, G., R.M. Rasmussen, K. Manning, 2004: Explicit forecasts of winter precipitation using an improved bulk microphysics scheme. Part I: Description and sensitivity analysis. *Mon. Wea. Rev*., **132**, 519-542.

———, P.R. Field, R.M. Rasmussen, W.D. Hall, 2008: Explicit forecasts of winter precipitation using an improved bulk microphysics scheme. Part II: Implementation of a new snow parameterization. *Mon. Wea. Rev.*, **136**, 5095-5115.

Van Weverberg, K., A.M. Vogelmann, H. Morrison, J.A. Milbrandt, 2012a: Sensitivity of idealized squall line simulations to the level of complexity used in two-moment bulk microphysics schemes. *Mon. Wea. Rev,* in press.

———, N.P.M. van Lipzig, L. Delobbe, A.M. Vogelmann, 2012b: The role of precipitation size distributions in km-scale NWP simulations of intense precipitation: Evaluation of cloud properties and surface precipitation. *Quart. J. Roy. Meteor. Soc,* submitted.

Varble, A., A.M. Fridlind, E.J. Zipser, A.S. Ackerman, J.-P. Chaboureau, J. Fan, A. Hill, S.A. McFarlane, J.-P. Pinty, B. Shipway, 2011: Evaluation of cloud-resolving model

intercomparison simulations using TWP-ICE observations: Precipitation and cloud structure. *J. Geophys. Res*., **116**, doi:10.1029/2010JD015180.

Wang, Y., C.N. Long, L.R. Leung, J. Dudhia, S.A. McFarlane, J.H. Mather, S.J. Ghan, X. Liu, 2009: Evaluating regional cloud-permitting simulations of the WRF model for the Tropical Warm Pool International Cloud Experiment (TWP-ICE), Darwin, 2006. *J. Geophys. Res*., **114**, doi:10.1029/2009JD012729.

Wright, J.S., R. Fu, A.J. Heymsfield, 2009: A statistical analysis of the influence of deep convection on water vapour variability in the tropical upper troposphere. *Atmos. Chem. Phys*., **9**, 5847-5864.

Wu, J., A.D. DelGenio, M.-S. Yao, A.B. Wolf, 2009: WRF and GISS SCM simulations of convective updraft properties during TWP-ICE. *J. Geophys. Res*., **114**, doi:10.1029/2008JD010851.

Yuan, J., R.A. Houze Jr., 2010: Global variability of mesoscale convective system anvil structure from A-train satellite data. *J. Climate*, **23**, 5864-5888.

Yuter, S.E., R.A. Houze, E.A. Smith, T.T. Wilheit, E. Zipser, 2005: Physical characterization of tropical oceanic convection observed in KWAJEX. *J. Appl. Meteor*., **44**, 385-415.

Zhou, Y.P., W.-K. Tao, A.Y. Hou, W.S. Olson, C.-L. Shie, K.-M. Lau, M.-D. Chou, X. Lin, M. Grecu, 2007: Use of high-resolution satellite observations to evaluate cloud and precipitation statistics from cloud-resolving model simulations. Part I: South China sea monsoon experiment. *J. Atmos. Sci*., **64**, 4309-4329.

7. Figure Captions

Figure 1: Model domains used for all three simulation experiments over the Tropical Western Pacific (TWP). Successive 20-km and 4-km nested domains are denoted by the inner solid rectangles. The dashed rectangle shows the TWP domain for which GOES-9 satellite data were available. Latitudes and longitudes are indicated by the numbers in the margins. The analysis domain is defined as the common area between the 4-km model domain and the TWP domain.

Figure 2: Fall speed – diameter (V-D) relations for the precipitating hydrometeor species in the three microphysics schemes, as inferred from the constants provided in Table 1. Note that while the X-axis ranges from 0 to 6 mm for rain, snow and graupel, it ranges from 0 to 0.6 mm for cloud ice.

Figure 3: Snapshots of the spatial distribution of cloud types at 3 UTC on 29 December 2003 as observed by GOES-9 (top left) and as simulated by the three microphysics schemes. Cloud types (see text) were defined based on the ISCCP classification technique, using CTP and COT and are denoted by the colors as indicated by the legend; land masses are grey. Thick black contours denote those cloud fields identified as MCSs. Latitudes and longitudes are indicated by the numbers in the margins.

Figure 4: Histograms of the 6-day averaged total area covered within the analysis domain by each of the ISCCP cloud classes (see text) in the observations (GOES) and each of the microphysics experiments. Bars represent the time-averaged coverage of each cloud class and the colors are in accordance with Figure 3. The hatched area denotes the horizontal area of each cloud class that was associated with an MCS.

Figure 5: Box-whisker plots of the size distribution of MCSs as identified in the observations and each of the microphysics experiments for the entire simulation period and domain. Boxes are limited by the 25^{th} and 75^{th} percentiles of the distribution and whiskers extend out to the 5^{th} and 95^{th} percentiles; the center lines are the medians. Separate statistics are provided for the entire MCS (top), core regions (middle) and anvil regions (bottom), which were defined based on BT as in the definitions of Laing and Fritsch (1993) and determined using the detection-and-spread method used in the cloud-tracking algorithm.

Figure 6: Vertical profiles of updraft properties, averaged over the entire simulation period and domain for each of the microphysics experiments. Top panels provide total updraft mass-flux (a) and average updraft speed (b) for updrafts associated with MCS core regions only. The bottom panels provide domain total updraft mass-flux (c) and average updraft speed (d). Updrafts were defined based on a 1 m s^{-1} threshold.

Figure 7: Vertical profiles of individual updraft characteristics, averaged over the entire simulation time and domain for each of the microphysics experiments. Provided are the average size of *individual* updrafts (a), the number of individual updrafts (b), and the total area covered by *all* updrafts (c). Updrafts were defined based on a 1 m s^{-1} threshold.

Figure 8: Vertical profiles of cloud ice characteristics, averaged over the entire simulation time and over MCS core regions only for all of the microphysics experiments. Panels denote (a) the mixing ratio (Q_I), (b) number concentration (N_I), (c) mass-weighted mean diameter (D_{MI}), and (d) fall velocity (V_I).

Figure 9: As in Figure 8, but for the snow species denoted by the subscript S.

Figure 10: As in Figure 8, but for the graupel species denoted by the subscript G.

Figure 11: Probability density functions of snow mixing ratio (Q_S) versus snow fall velocity (V_S) in the three microphysics experiments, based on simulated snow properties of all domain grid cells that are above 10 km. The banded features in WSM6 and THOM are caused by the temperature dependency of the N_{0S} parameter and hence reflect the different model levels.

Figure 12: Vertical cross sections through the most northeastern MCS depicted in Figure 3 along the domain-mean wind vector for WSM6 (top), MORR (middle) and THOM (bottom). For each experiment, the cross sections were taken across the 25 strongest MCS updrafts. All cross sections were subsequently centered on the main updraft and averaged into the cross section shown. The left hand panels denote the dynamic features of the MCSs. Colored shading indicates the deviation of wind speed from the mean wind speed at each level. Blue colors indicate air masses diverging from the updraft in the center (at 800 km), while red colors indicate convergence towards the main updraft. Arrows indicate the deviation of wind vectors from the mean vector over all levels. The largest arrows correspond to about 10 m s^{-1}. Contours on the left-hand panels depict the snow sedimentation velocities (contours are drawn every 0.3 m s^{-1}). The extinction coefficient is shown on the right hand panels as grey shading. Contours on these panels are the relative humidity with respect to ice (contours drawn every 10% from 75% to 95%).

Figure 13: Spatial distribution of 6-day surface precipitation accumulations as observed by the GPCP and as simulated by all microphysics schemes. Observations have a grid spacing of $1° \times 1°$ and simulated precipitation fields were aggregated from the original 4 km grid spacing to the observed grid spacing for comparison. Latitudes and longitudes are indicated by the numbers in the margins.

Figure 14: Vertical profiles of downdraft properties, averaged over the entire simulation period and domain for each of the microphysics experiments. Provided are the total downdraft mass flux (a), the mean downdraft speed (b), and the maximum downdraft speed (c). Downdrafts were defined based on a -1 m s^{-1} threshold.

Figure 15: Vertical profiles of downdraft hydrometeor characteristics. Profiles are averaged over the entire simulation time for downdrafts associated with surface precipitation rates exceeding 20 mm hr^{-1} for the three microphysics experiments. The panels denote (left) the mixing ratio (Q_X), and (right) mass-weighted mean size (D_X) for, respectively, rain (top), snow (middle), and graupel (bottom). The domain- and time-averaged freezing levels are denoted by the crosses. Downdrafts were defined based on a -1 m s^{-1} threshold.

Table 1: Overview of the primary differences in terms of particle size distributions between the three cloud microphysics schemes investigated in this study. Given are the shape of the distribution (negative exponential or gamma), the intercept (N_{0X}), constants a_{mx} and b_{mx} for the mass-diameter relations, constants a_{vx} and b_{vs} for the velocity-diameter relations, and the particle density (ρ_x). References for each of the variables are provided below the table.

Scheme	Species	Shape	N_{0X} (m^{-1})	a_{mx} (kg $m^{-b_{mx}}$)	b_{mx}	a_{vx} (m^{s-1} $m^{-b_{vx}}$)	b_{vx}	ρ_x (kg m^{-3})
WSM6	Rain	EXP	8×10^6	$\frac{\pi\rho_r}{6}$	3.	841.9 [*]	0.8 [*]	1000.
	Snow	EXP	$\min\left[2\times10^8, 2\times10^6\times\exp\left[0.12(T_0-T)\right]\right]$ [$]	$\frac{\pi\rho_s}{6}$	3.	11.72 [¶]	0.41 [¶]	100.
	Graupel	EXP	4×10^6	$\frac{\pi\rho_g}{6}$	3.	330. [¶]	0.8 [¶]	500.
	Ice[1]	EXP	-	-	-	-	-	-
THOM	Rain	EXP	$\left(\frac{N_1-N_2}{2}\right)\tanh\left[\frac{(q_{r0}-q_r)}{4q_{r0}}\right]+\frac{N_1+N_2}{2}$ [§]	$\frac{\pi\rho_r}{6}$	3.	4854.4 [@,2]	1. [@,2]	1000.
	Snow	EXP+GAM	$\min\left[2\times10^8, 2\times10^6\times\exp\left[0.12(T_0-T)\right]\right]$ [$]	0.069 [£]	2. [£]	40. [§,2]	0.55 [§,2]	100.
	Graupel	EXP	$\max\left[10^4, \min\left(\frac{200}{q_o}, 5\times10^6\right)\right]$ [§]	$\frac{\pi\rho_g}{6}$	3.	442. [~]	0.89 [~]	400.
	Ice	EXP	PROGNOSTIC	$\frac{\pi\rho_i}{6}$	3.	1847.5 [§]	1. [§]	890.
MORR	Rain	EXP	PROGNOSTIC	$\frac{\pi\rho_r}{6}$	3.	841.9 [*]	0.8 [*]	1000.
	Snow	EXP	PROGNOSTIC	$\frac{\pi\rho_s}{6}$	3.	11.72 [¶]	0.41 [¶]	100.
	Graupel	EXP	PROGNOSTIC	$\frac{\pi\rho_g}{6}$	3.	19.3 [#]	0.37 [#]	400.
	Ice	EXP	PROGNOSTIC	$\frac{\pi\rho_i}{6}$	3.	700. [&]	1. [&]	500.

[1] N_i in WSM6 is derived as a function of q_i: $N_i = c(\rho q_i)^d$ where c and d are constants. V_i is also a function of q_i, following Heymsfield and Donner (1990)

[2] V_s and V_r in THOM follow Ferrier (1994) and are given by $V_x = a_{vx} D^{b_{vx}} \exp(-fD)$, where f is 195 and 125 for rain and snow respectively

[*] Liu and Orville (1969) [¶] Locatelli and Hobbs (1974) [@] Ferrier 1994

[§] Thompson et al. (2008) [~] Heymsfield and Kajikawa (1987) [#] Ferrier et al. (1995)

[&] Morrison et al. (2009) [£] Cox (1988) [$] Houze et al. (1979)

Table 2: Cloud fractions of the analysis domain (see Fig. 1), occupied by high clouds, middle clouds and low clouds in the observations and the model simulations. Cloud fractions were averaged over all output times (hourly), provided that the solar zenith angle was less than 70°. Cloud fraction for the domain are given (bold numbers), as well as the fraction of the total that are within the MCSs. The last column lists the total cloud fraction (bold) and the total MCS fraction for the entire domain.

	High Clouds (%)		Middle Clouds (%)		Low Clouds (%)		Total (%)	
	Total	MCS	Total	MCS	Total	MCS	Total	MCS
GOES	**45**	96	**5**	4	**2**	0	**53**	22
WSM6	**16**	74	**6**	16	**15**	10	**37**	9
MORR	**22**	88	**7**	9	**10**	3	**39**	11
THOM	**43**	94	**4**	3	**11**	3	**58**	35

Table 3: Statistics of the MCSs tracked in the observations and the simulations for the analysis domain and simulation period. Provided are the total number of individual MCS tracks. The average size, BT, and COT are given for the MCSs, and also separately for the MCS core and anvil regions, based on the Laing and Fritsch (1993) definitions and determined using the detection-and-spread method used in the cloud-tracking algorithm.

	# Tracks	Size (10^5 km^2)			BT (K)			COT		
		Core	Anvil	Total	Core	Anvil	Total	Core	Anvil	Total
GOES	**31**	1.6	7.1	**8.7**	211.0	257.0	**248.5**	27.0	6.5	**8.4**
WSM6	**18**	1.1	5.9	**6.9**	215.1	237.3	**232.8**	23.5	20.0	**20.7**
MORR	**16**	1.2	5.6	**6.8**	214.9	238.8	**234.1**	28.9	19.6	**21.4**
THOM	**32**	5.0	8.3	**13.3**	213.2	237.8	**227.7**	31.0	16.6	**22.5**

Table 4: Mean and maximum 6-day surface precipitation accumulations (SP), averaged over the entire domain as observed (GPCP) and as simulated by each experiment. All simulated precipitation amounts were aggregated to the GPCP 1° × 1° grid for comparison. The last column provides the fractional coverage of surface precipitation for the entire domain for only grid cells that with precipitation accumulations of more than 10 mm.

	Mean SP (mm)	Maximum SP (mm)
GPCP	39.1	217.1
WSM6	80.8	476.3
MORR	68.1	370.4
THOM	89.5	530.9

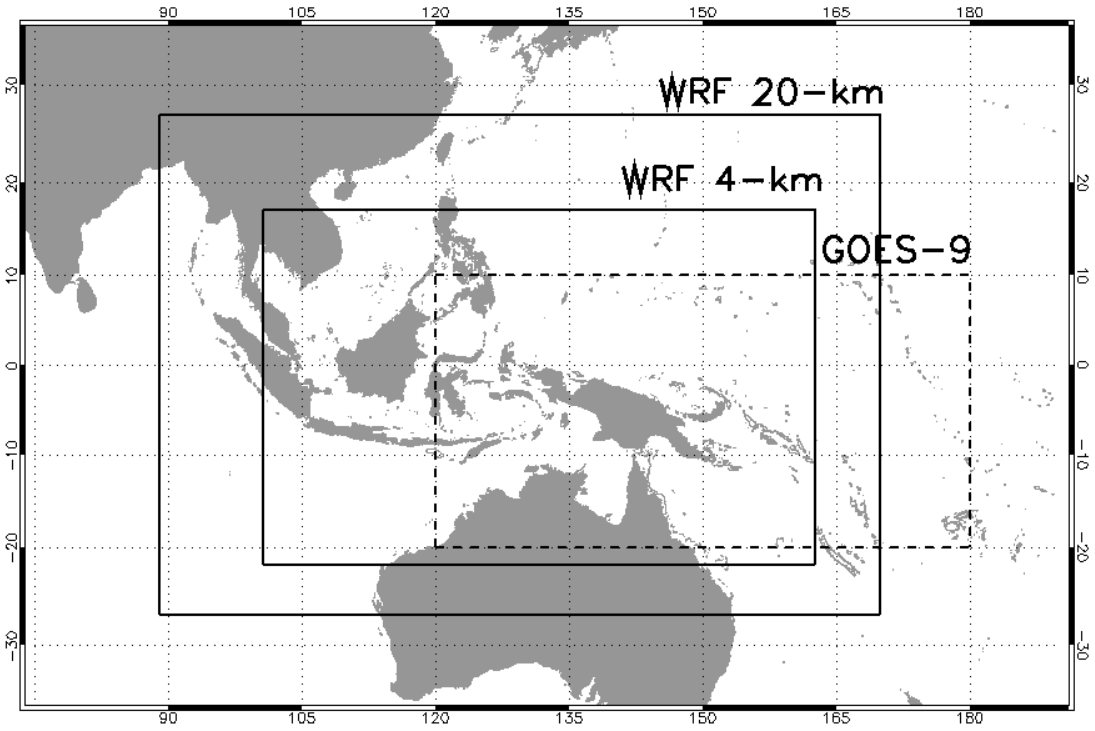

Figure 1: Model domains used for all three simulation experiments over the Tropical Western Pacific (TWP). Successive 20-km and 4-km nested domains are denoted by the inner solid rectangles. The dashed rectangle shows the TWP domain for which GOES-9 satellite data were available. Latitudes and longitudes are indicated by the numbers in the margins. The analysis domain is defined as the common area between the 4-km model domain and the TWP domain.

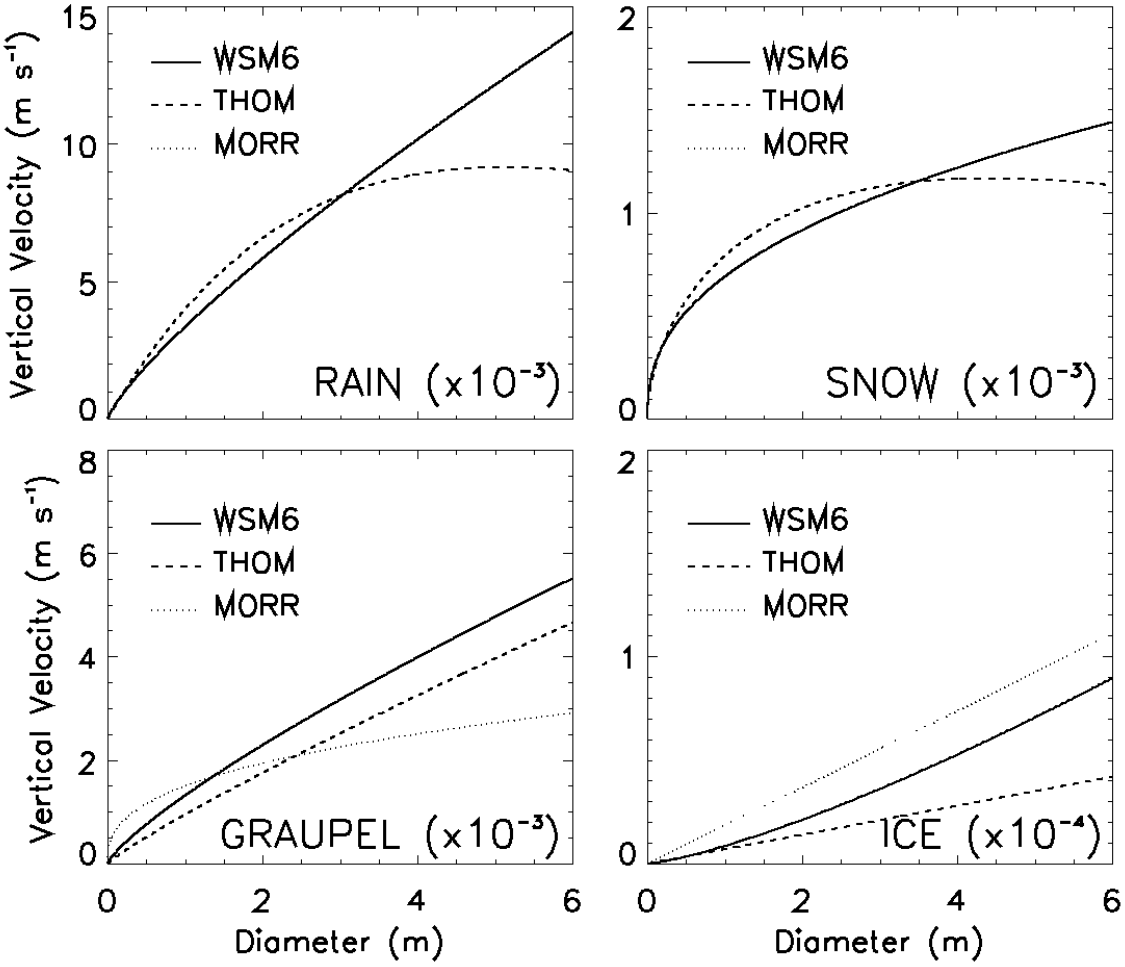

Figure 2: Fall speed – diameter (V-D) relations for the precipitating hydrometeor species in the three microphysics schemes, as inferred from the constants provided in Table 1. Note that while the X-axis ranges from 0 to 6 mm for rain, snow and graupel, it ranges from 0 to 0.6 mm for cloud ice. MORR and WSM6 have identical rain and snow V-D relations and hence overlay each other.

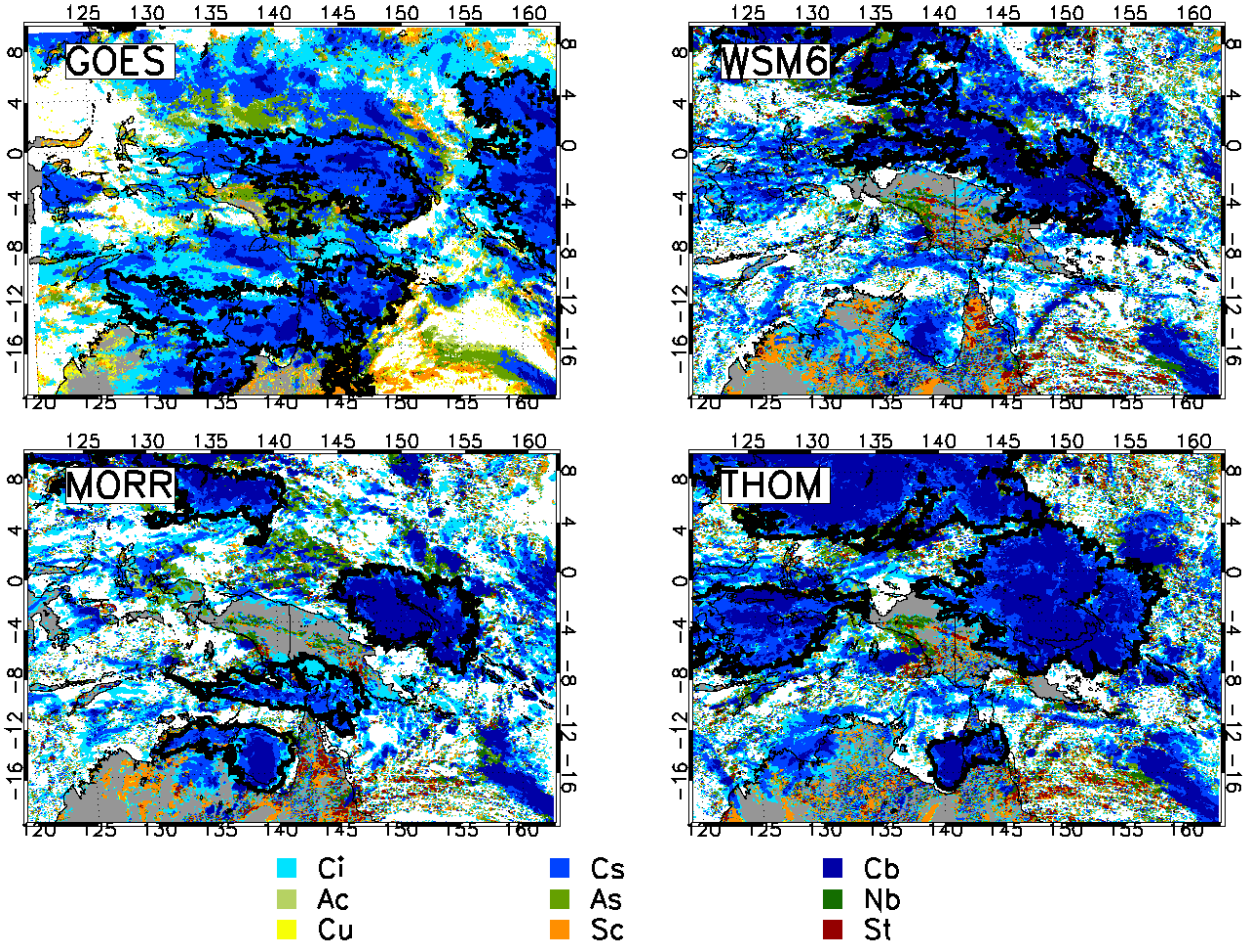

Figure 3: Snapshots of the spatial distribution of cloud types at 3 UTC on 29 December 2003 as observed by GOES-9 (top left) and as simulated by the three microphysics schemes. Cloud types (see text) were defined based on the ISCCP classification technique, using CTP and COT and are denoted by the colors as indicated by the legend; land masses are grey. Thick black contours denote those cloud fields identified as MCSs. Latitudes and longitudes are indicated by the numbers in the margins.

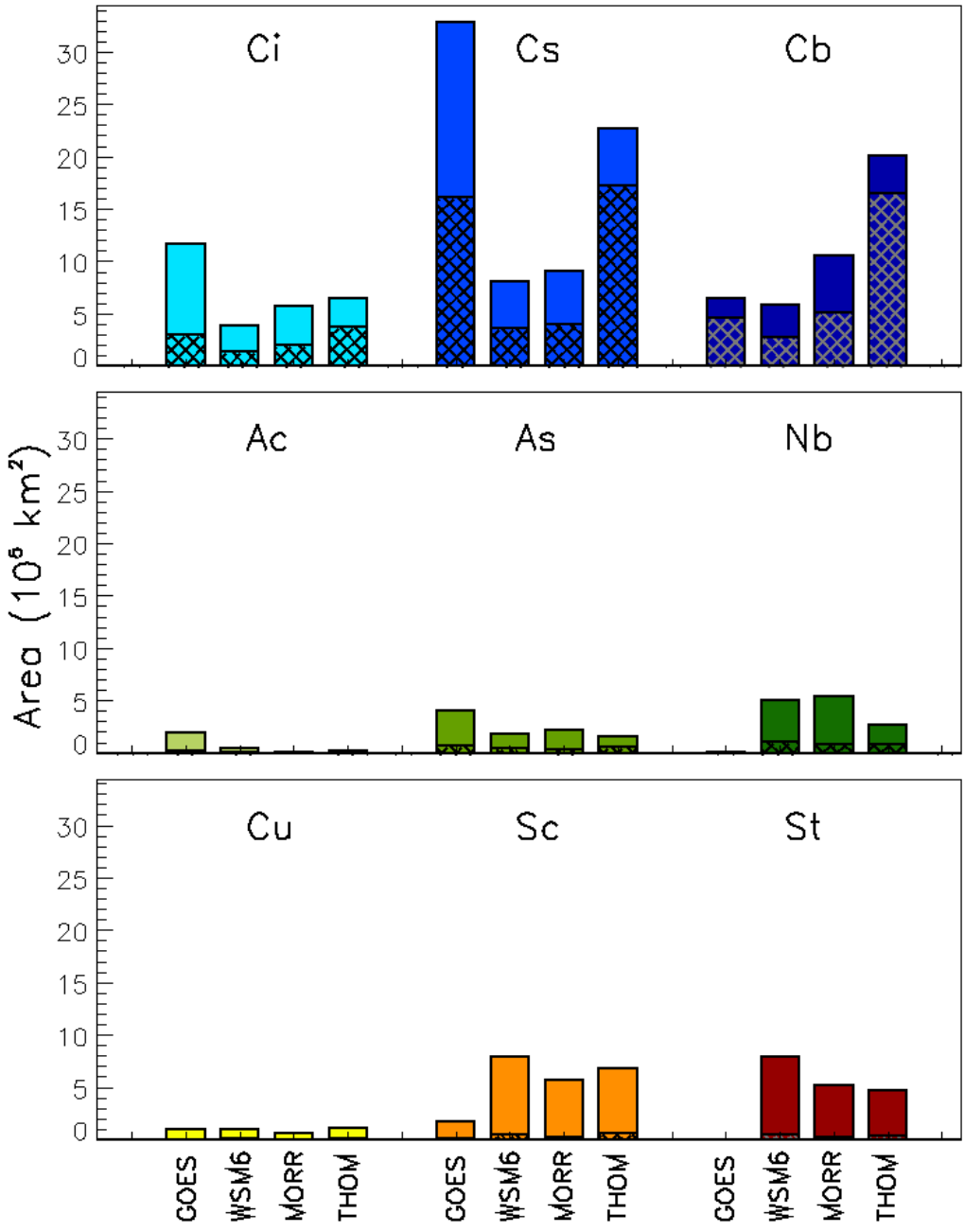

Figure 4: Histograms of the 6-day averaged total area covered within the analysis domain by each of the ISCCP cloud classes (see text) in the observations (GOES) and each of the microphysics experiments. Bars represent the time-averaged coverage of each cloud class and the colors are in accordance with Figure 3. The hatched area denotes the horizontal area of each cloud class that was associated with an MCS.

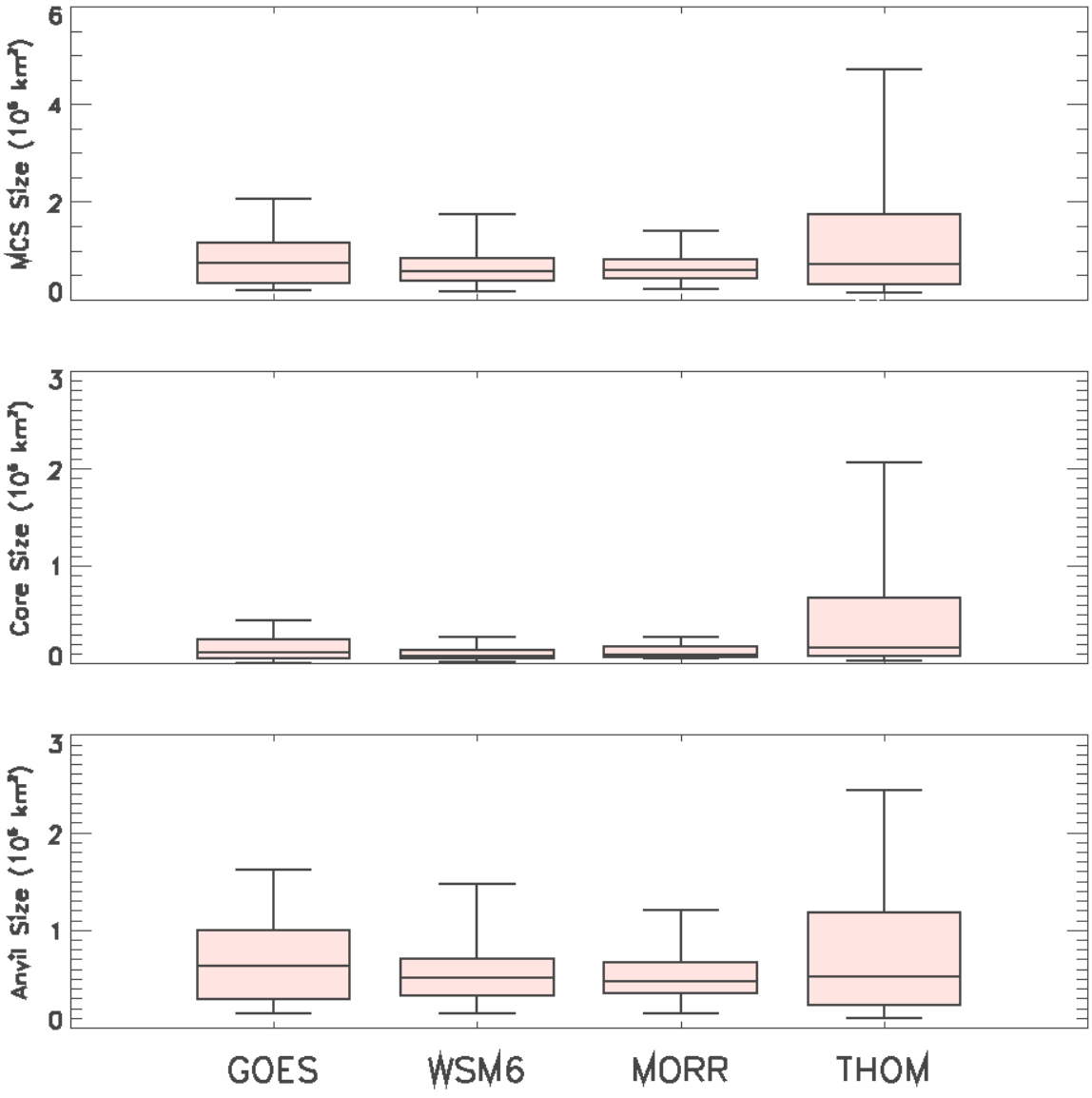

Figure 5: Box-whisker plots of the size distribution of MCSs as identified in the observations and each of the microphysics experiments for the entire simulation period and domain. Boxes are limited by the 25th and 75th percentiles of the distribution and whiskers extend out to the 5th and 95th percentiles; the center lines are the medians. Separate statistics are provided for the entire MCS (top), core regions (middle) and anvil regions (bottom), which were defined based on BT as in the definitions of Laing and Fritsch (1993) and determined using the detection-and-spread method used in the cloud-tracking algorithm.

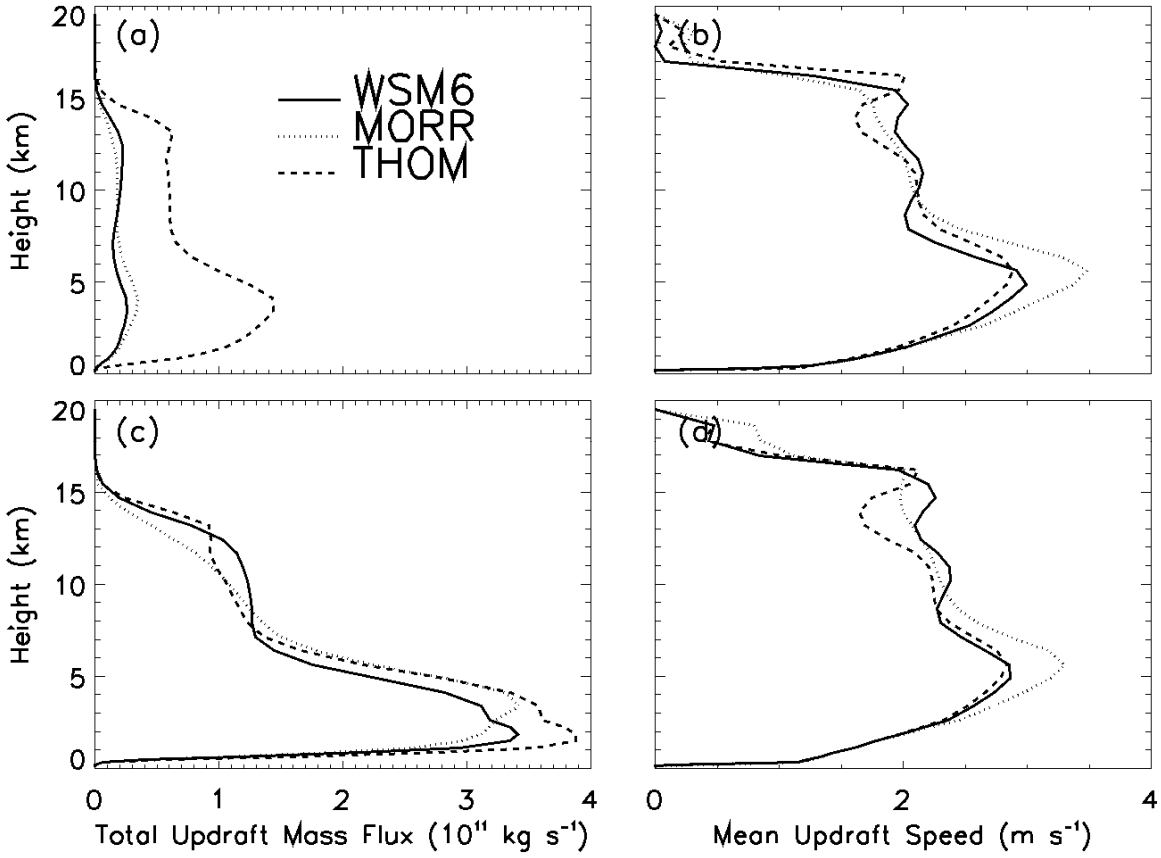

Figure 6: Vertical profiles of updraft properties, averaged over the entire simulation period and domain for each of the microphysics experiments. Top panels provide total updraft mass-flux (a) and average updraft speed (b) for updrafts associated with MCS core regions only. The bottom panels provide domain-total updraft mass-flux (c) and average updraft speed (d). Updrafts were defined based on a 1 m s^{-1} threshold.

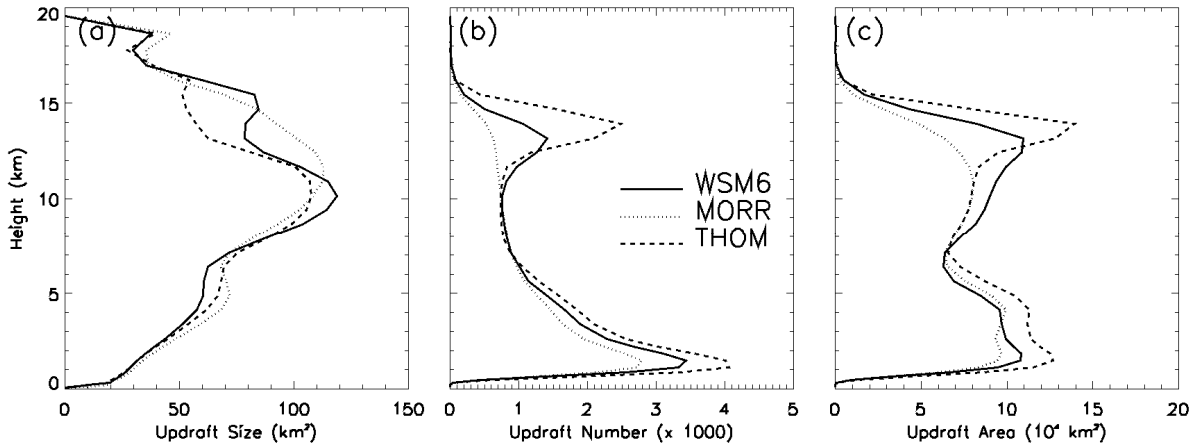

Figure 7: Vertical profiles of individual updraft characteristics, averaged over the entire simulation time and domain for each of the microphysics experiments. Provided are the average size of *individual* updrafts (a), the number of individual updrafts (b), and the total area covered by *all* updrafts (c). Updrafts were defined based on a 1 m s^{-1} threshold.

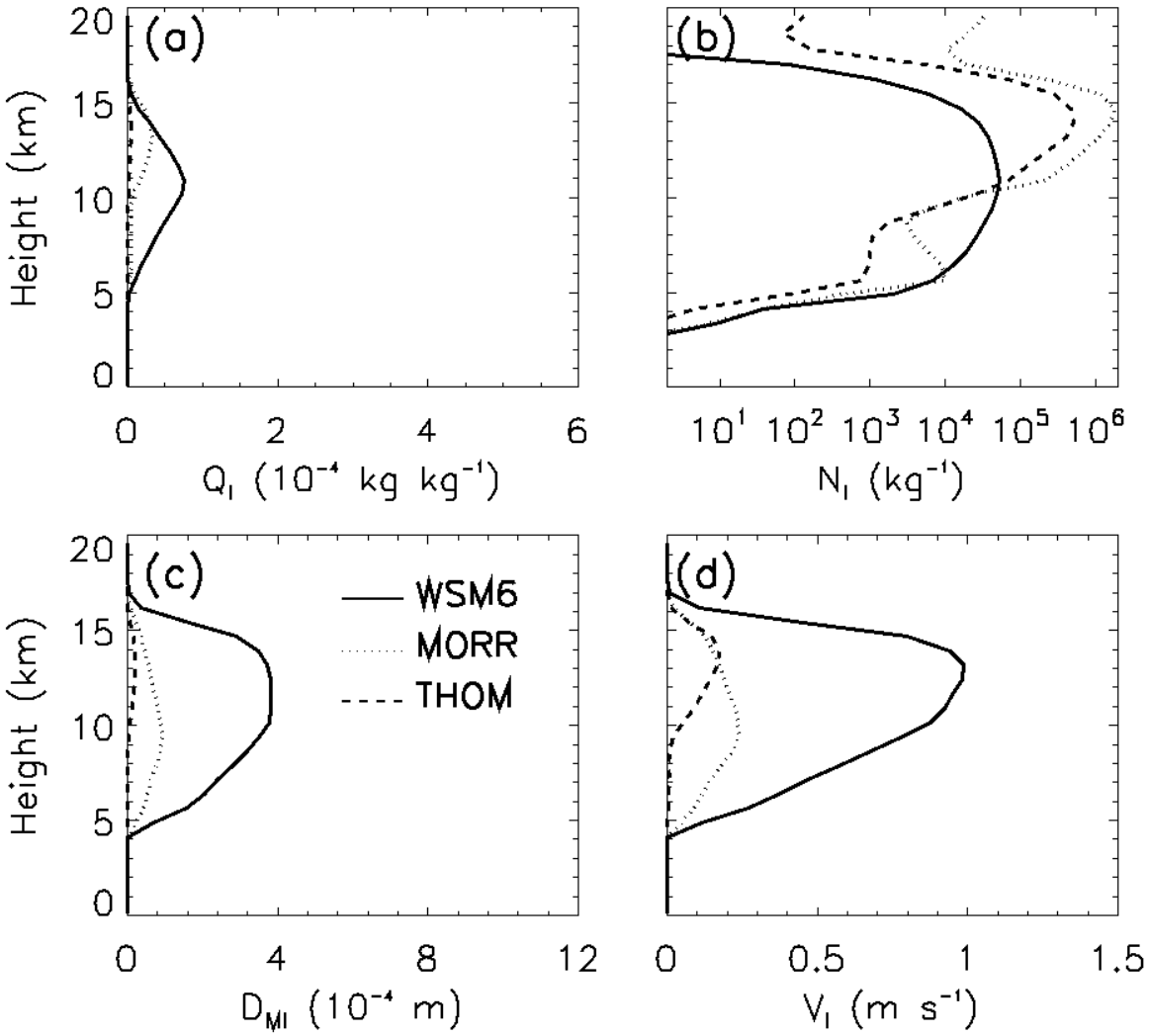

Figure 8: Vertical profiles of cloud ice characteristics, averaged over the entire simulation time and over MCS core regions only for all of the microphysics experiments. Panels denote (a) the mixing ratio (Q_I), (b) number concentration (N_I), (c) mass-weighted mean diameter (D_{MI}), and (d) fall velocity (V_I).

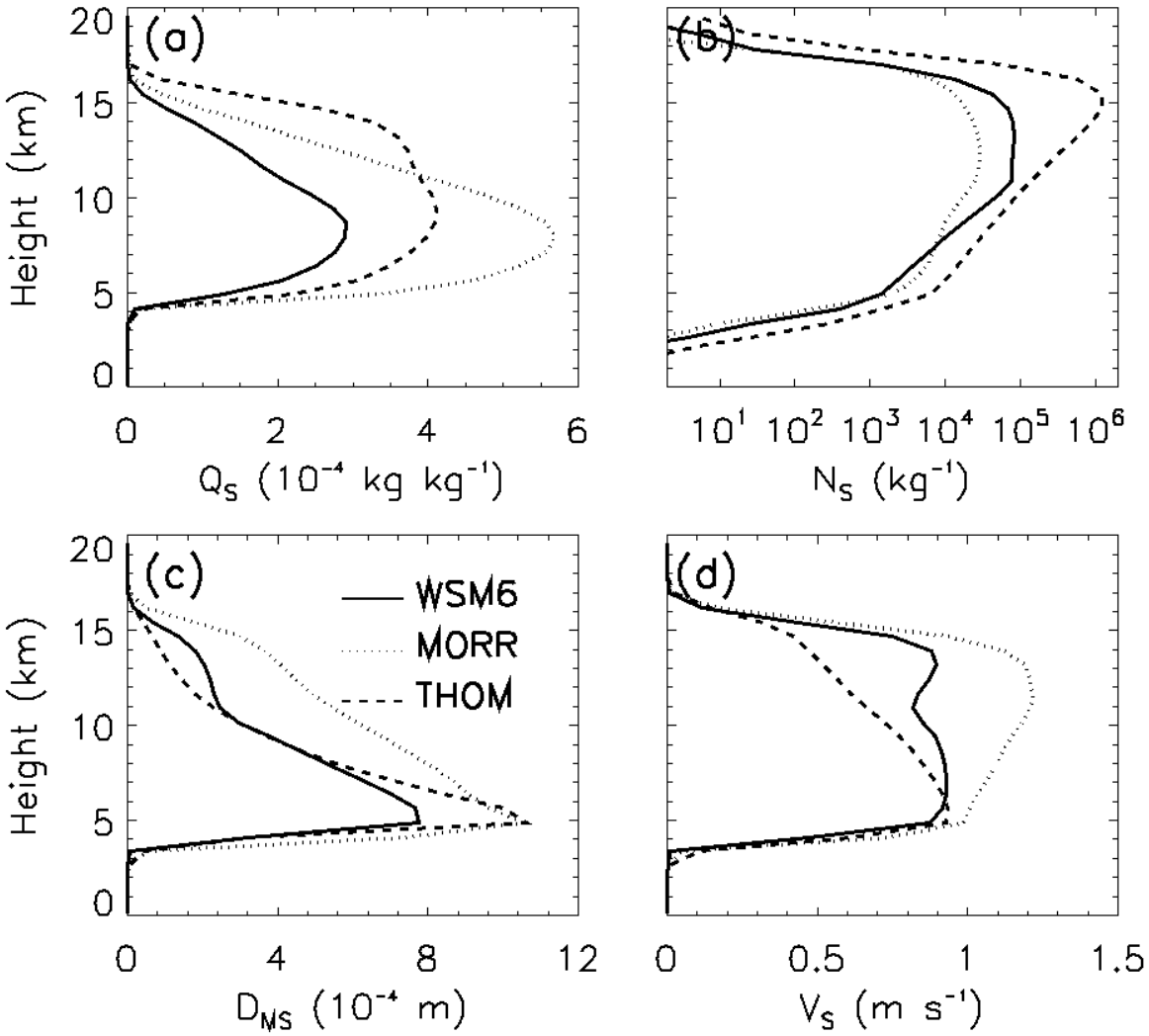

Figure 9: As in Figure 8, but for the snow species denoted by the subscript S.

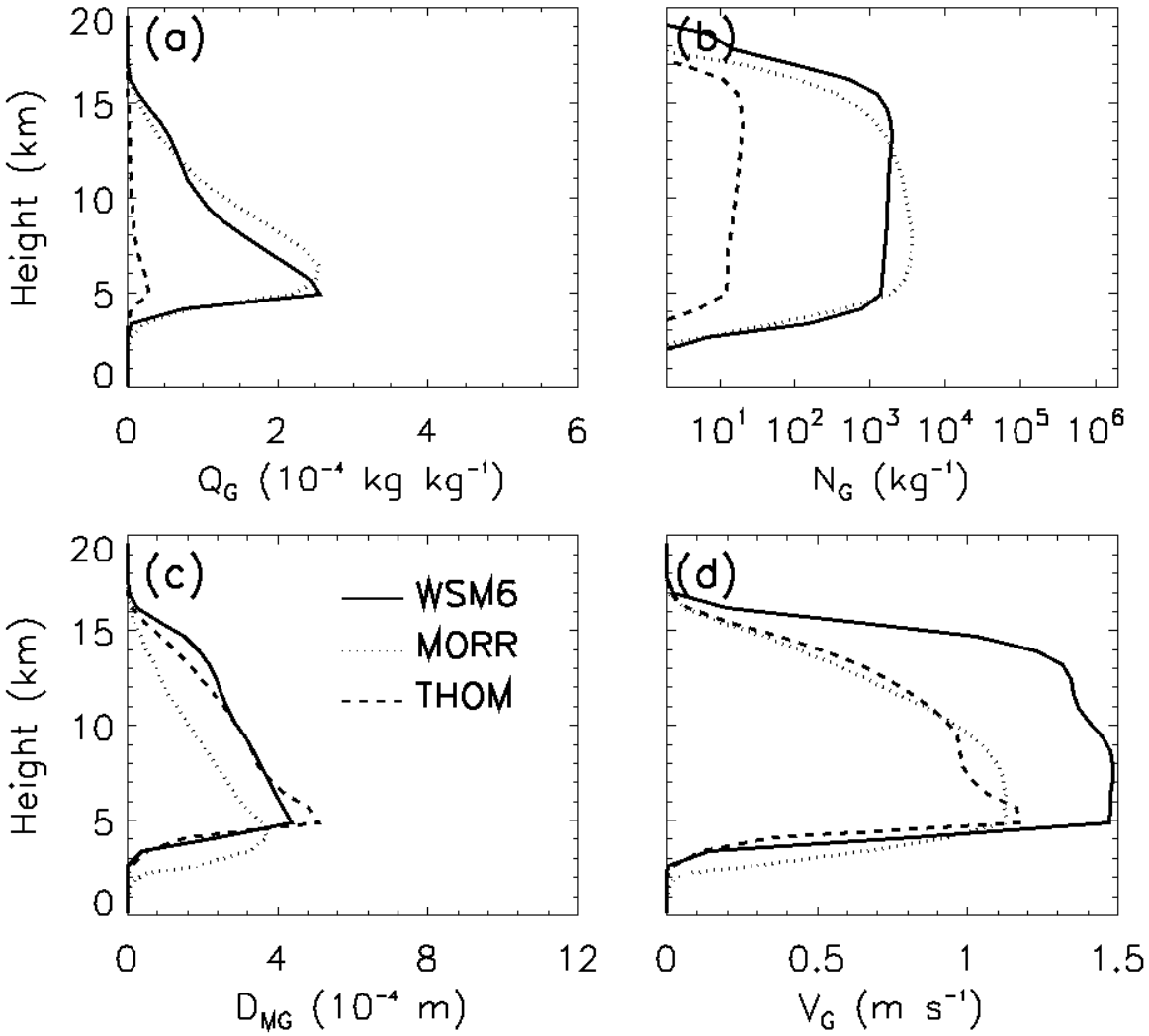

Figure 10: As in Figure 8, but for the graupel species denoted by the subscript G.

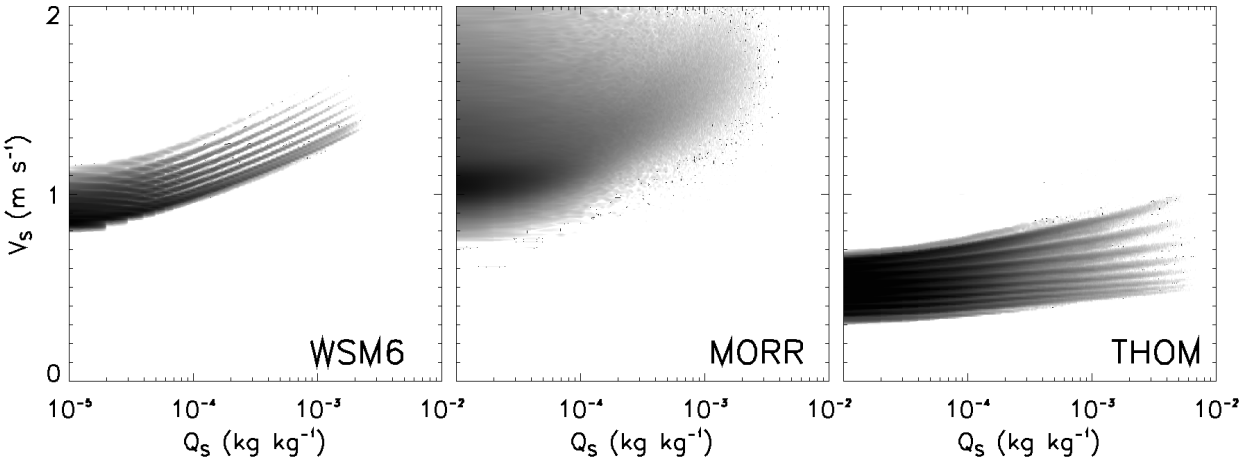

Figure 11: Probability density functions of snow mixing ratio (Q_S) versus snow fall velocity (V_S) in the three microphysics experiments, based on simulated snow properties of all domain grid cells that are above 10 km. The banded features in WSM6 and THOM are caused by the temperature dependency of the N_{0S} parameter and hence reflect the different model levels.

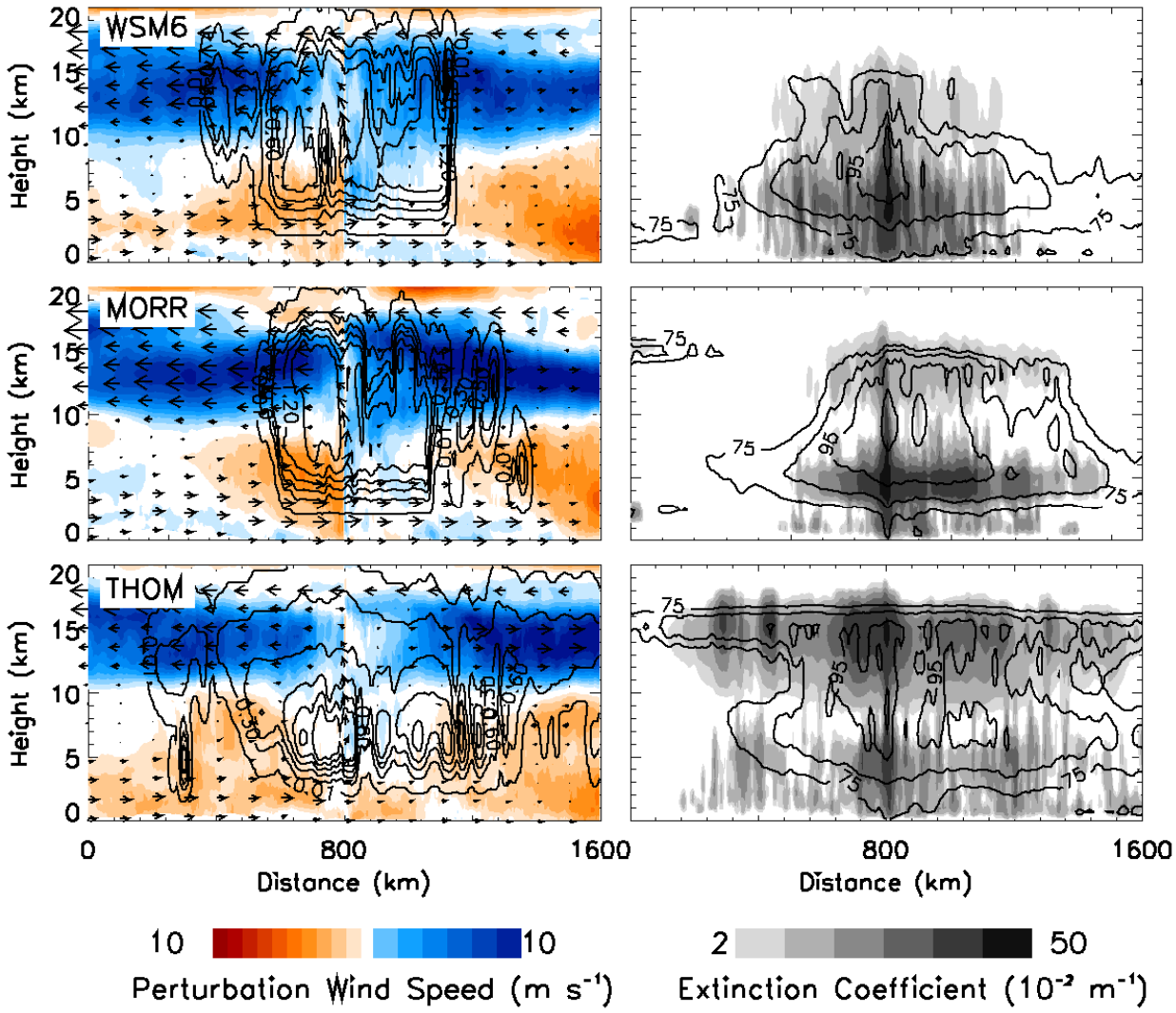

Figure 12: Vertical cross sections through the most northeastern MCS depicted in Figure 3 along the domain-mean wind vector for WSM6 (top), MORR (middle) and THOM (bottom). For each experiment, the cross sections were taken across the 25 strongest MCS updrafts. All cross sections were subsequently centered on the main updraft and averaged into the cross section shown. The left hand panels denote the dynamic features of the MCSs. Colored shading indicates the deviation of wind speed from the mean wind speed at each level. Blue colors indicate air masses diverging from the updraft in the center (at 800 km), while red colors indicate convergence towards the main updraft. Arrows indicate the deviation of wind vectors from the mean vector over all levels. The largest arrows correspond to about 10 m s^{-1}. Contours on the left-hand panels depict the snow sedimentation velocities (contours are drawn every 0.3 m s^{-1}). The extinction coefficient is shown on the right hand panels as grey shading. Contours on these panels are the relative humidity with respect to ice (contours drawn every 10% from 75% to 95%).

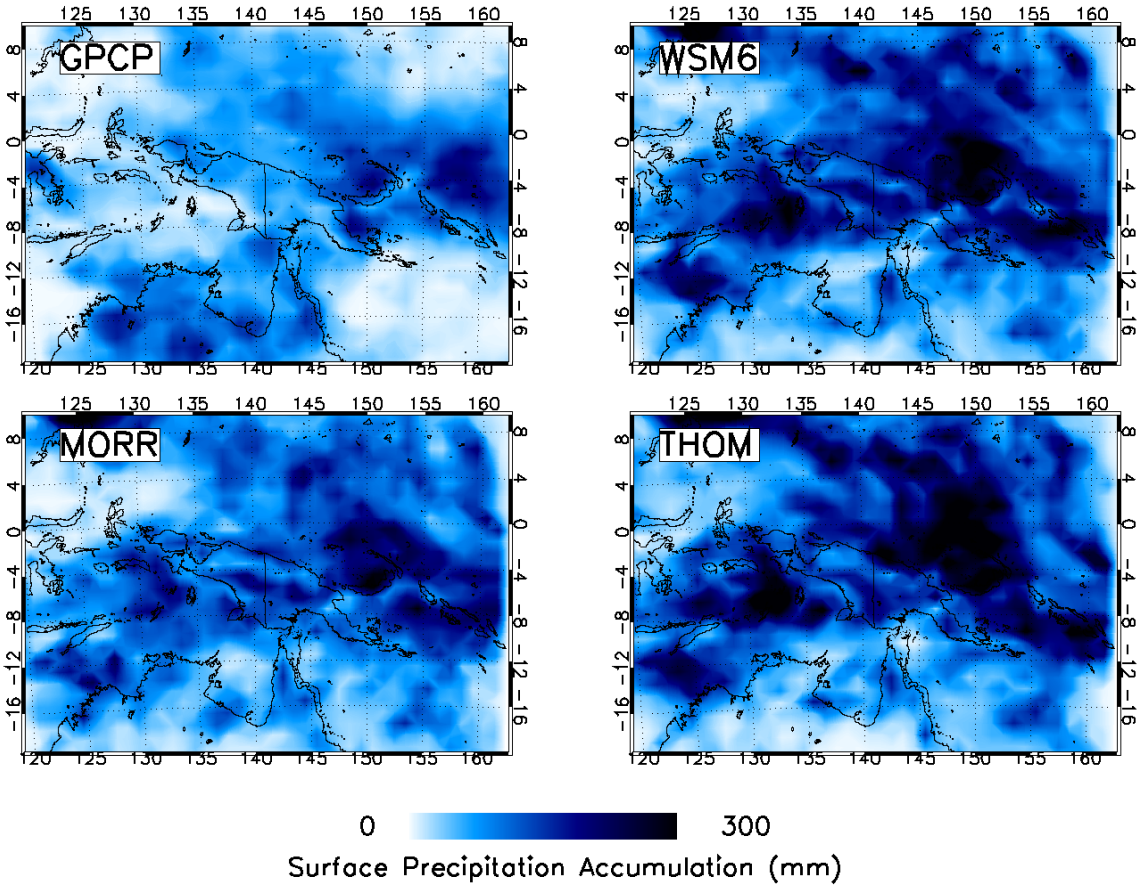

Figure 13: Spatial distribution of 6-day surface precipitation accumulations as observed by the GPCP and as simulated by all microphysics schemes. Observations have a grid spacing of 1° × 1° and simulated precipitation fields were aggregated from the original 4 km grid spacing to the observed grid spacing for comparison. Latitudes and longitudes are indicated by the numbers in the margins.

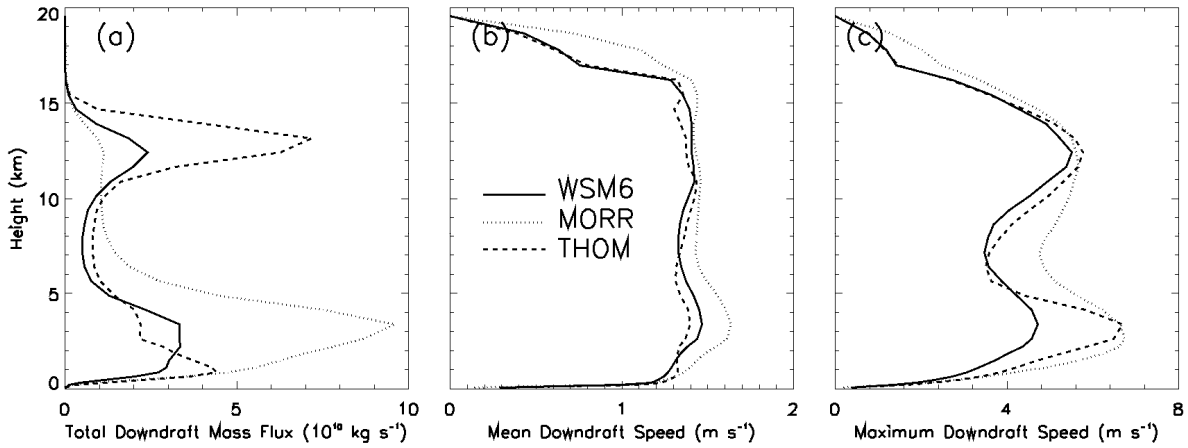

Figure 14: Vertical profiles of downdraft properties, averaged over the entire simulation period and domain for each of the microphysics experiments. Provided are the total downdraft mass flux (a), the mean downdraft speed (b), and the maximum downdraft speed (c). Downdrafts were defined based on a -1 m s^{-1} threshold.

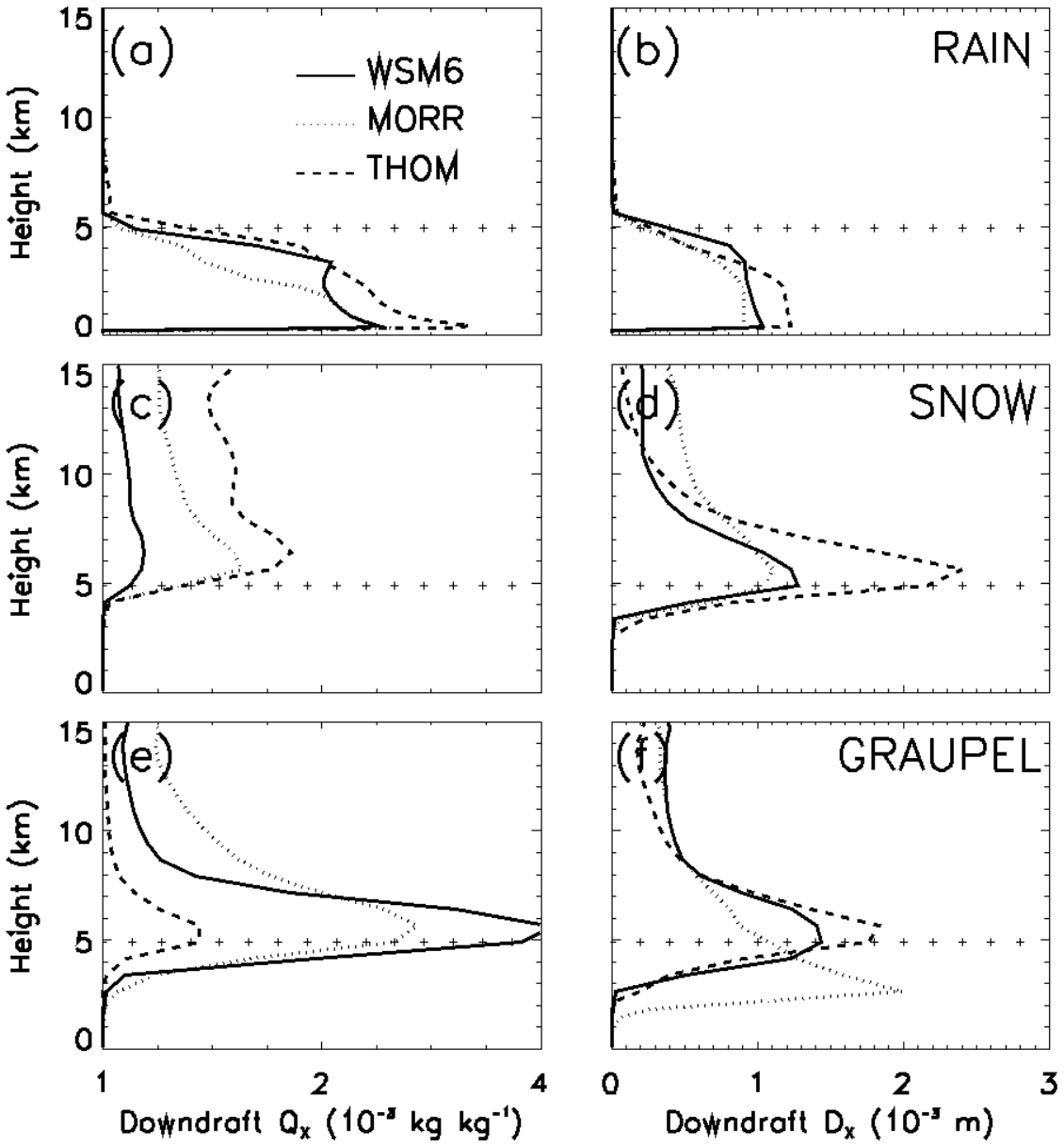

Figure 15: Vertical profiles of downdraft hydrometeor characteristics. Profiles are averaged over the entire simulation time for downdrafts associated with surface precipitation rates exceeding 20 mm hr^{-1} for the three microphysics experiments. The panels denote (left) the mixing ratio (Q_X), and (right) mass-weighted mean size (D_X) for, respectively, rain (top), snow (middle), and graupel (bottom). The domain- and time-averaged freezing levels are denoted by the crosses. Downdrafts were defined based on a -1 m s^{-1} threshold.